Kidney disease reprograms microbiome-host signaling to promote heart failure

Alex Yarritu[1,2,3,4,*], Wibke Anders[1,2,3,4,5,*], Arne Thiele[1,2,3,4], Olena Potapenko[1,2,3,4], Fabian Schumacher[5], István A. Szijártó[1,2,3,4], Ariana Matz-Rauch[1,2,3,4], Jakob Versnjak[6], Natnael Gebremedhin[1,2,3,4], Victoria McParland[1,2,3,4], Simon Heckscher[7], Sakshi Kamboj[7], Giuseppe Trimarchi[3,8], Harithaa Anandakumar[1,2,3,4], Franziska Fuckert[1,2,3,4], Carina Hoffmann[1], Sara A. Hassan[1,5], Paul M. Bonnekoh[1,2,3,4], Moritz I. Wimmer[1,2,3,4], Felix Behrens[1,2,3,4], Jakob Voelkl[3,4,9], Rafael Kramann[10], Ulrich Kintscher[3,8], Titus Kuehne[3,6,11], Burkhard Kleuser[5], Alma Zernecke[12], Peter J. Oefner[7], Wolfram Gronwald[7], Katja Dettmer[7], Kai-Uwe Eckardt[4], Dominik N. Müller[1,2,3,13], Marcus Kelm[3,6,11], Johannes Holle[1,2,3,14], Hendrik Bartolomaeus[2,3,12,†], Nicola Wilck[1,2,3,4,†]

[1]Experimental and Clinical Research Center (ECRC), a cooperation of Charité – Universitätsmedizin Berlin and Max Delbrück Center for Molecular Medicine, Berlin, Germany

[2]Max-Delbrück-Center for Molecular Medicine in the Helmholtz Association, Berlin, Germany

[3]DZHK (German Centre for Cardiovascular Research), partner site Berlin, Germany.

[4]Department of Nephrology and Medical Intensive Care, Charité – Universitätsmedizin Berlin, corporate member of Freie Universität Berlin and Humboldt-Universität zu Berlin, Berlin, Germany

[5]Freie Universität Berlin, Department of Biology, Chemistry and Pharmacy, Institute of Pharmacy, Berlin, Germany

[6]Institute of Computer-assisted Cardiovascular Medicine, Deutsches Herzzentrum der Charité, Berlin, Germany

[7]Institute of Functional Genomics, University of Regensburg, Regensburg, Germany

[8]Max Rubner Center for Cardiovascular Metabolic Renal Research, Institute of Pharmacology, Charité – Universitätsmedizin Berlin, Berlin, Germany

[9]Institute for Physiology and Pathophysiology, Johannes Kepler University of Linz, Linz, Austria

[10]Division of Nephrology and Clinical Immunology, University Hospital RWTH Aachen, Aachen, Germany
[11]Department of Congenital Heart Disease – Pediatric Cardiology, Deutsches Herzzentrum der Charité, Berlin, Germany
[12]Institute of Experimental Biomedicine, University Hospital Würzburg, Würzburg, Germany
[13]Charité – Universitätsmedizin Berlin, corporate member of Freie Universität Berlin and Humboldt-Universität zu Berlin, Berlin, Germany
[14]Department of General Pediatrics and Hematology/Oncology, University Children's Hospital, University Hospital Tübingen, Tübingen, Germany
*These authors contributed equally to this work.
†These authors contributed equally to this work.
Correspondence: nicola.wilck@charite.de

Summary

Gut microbiome-derived metabolites regulate host physiology, with systemic levels controlled by renal excretion. In kidney disease, impaired clearance leads to metabolite accumulation, inflammation, and secondary cardiovascular damage. We show that adverse cardiac remodeling following kidney disease critically depends on the microbiome. We identify microbiome-derived indoxyl sulfate-mediated activation of the aryl hydrocarbon receptor (AhR) as a key mechanism promoting IL-17A-producing T cells and cardiac fibrosis. AhR inhibition attenuates inflammation and cardiac remodeling. On population level, IL-17A is elevated in chronic kidney disease, particularly with coexisting heart failure. Mechanistically, AhR and IL-17A signaling induce a pro-fibrotic phenotype in cardiac fibroblasts, with conserved responses in human cells. This work identifies a microbiome-AhR-IL-17A axis as a mediator and druggable target of cardiovascular damage in kidney disease.

Introduction

Multimorbidity, the coexistence of two or more chronic conditions, is a major challenge for future medicine[1]. Secondary organ damage arises from a complex interplay between intrinsic physiological processes and environmental exposures. The crosstalk between the kidney, a key regulator of internal homeostasis, and the gut microbiome[2], a metabolically active interface between host and environment is particularly relevant. Chronic kidney disease (CKD), a growing global health burden[3], impairs the clearance of host- and microbiome-derived metabolites, leading to their accumulation and toxic effects[4,5]. Cardiovascular disease (CVD) is the most common comorbidity and the primary cause of mortality in CKD[6], with persistent low-grade inflammation recognized as a major but unaddressed driver of this pathology[7]. Although the gut microbiome strongly influences immunity[8], it is not yet targeted by standard CKD therapies. CKD is associated with an altered gut microbiome composition and production of metabolites entering the host circulation, including ligands of the aryl hydrocarbon receptor (AhR), a widely expressed transcription factor[9]. Indoxyl sulfate (IxS), a prototypical uremic toxin and agonistic AhR ligand, is derived from dietary tryptophan utilisation by gut microbes and hepatic sulfation. Upon ligation and activation, the AhR translocates to the nucleus to regulate gene expression and immune cell differentiation[10]. AhR signaling contributes to inflammation[11], but its effects vary with ligand type, concentration, and context[12].

Here, we examine how gut microbiome-immune system interactions drive adverse cardiac remodeling in kidney disease. We show that microbiome depletion confers protection, while IL-17A emerges as a microbiome-dependent driver of cardiac fibrosis and dysfunction in CKD. IL-17A is increased in CKD patients and even more so with coexisting heart failure. Bacterial metabolite IxS promotes T_H17 differentiation via the AhR, and in heart failure, induces T_H17 and aggravates cardiac remodeling. AhR inhibition suppresses T_H17 induction and cardiac fibrosis despite metabolite accumulation. We identify cardiac murine and human fibroblasts as AhR-modulated, IL-17A-responsive effectors. These findings reveal microbiome-dependent, pro-fibrotic pathways and position the AhR as a therapeutic target for cardiovascular protection in CKD.

Results

Gut microbiota accelerates cardiac remodeling in kidney disease

To assess the contribution of the gut microbiota to the host's response to kidney disease, we compared colonized and microbiome-depleted (oral antibiotics, Abx) 129/Sv mice subjected to subtotal nephrectomy (STNx), with Sham-operated mice as controls (Fig.1a). Disease progression was monitored over a 13-week period. Reduced 16S rRNA gene copies in cecal content confirmed successful microbiota depletion over the course of the experiment (Fig.S1a) and cecal weight was increased in Abx-treated mice, reminiscent of the germ-free (GF) mouse cecum (Fig.S1b)[13]. 16S rRNA gene sequencing of cecal samples from the non-microbiome-depleted groups showed a minor reduction in alpha diversity (Fig.S1c-e) in STNx mice while phyla composition remained similar (Fig.S1f). Principal component analysis (PCA) indicated a separation of bacterial communities (Fig.S1g). We found this to be due to an increase in known CKD-associated genera such as *Bacteroides* and *Ruminococcus* (Fig.S1h)[14]. Notably, the taxonomic shifts observed after STNx were less pronounced than those reported in patients with CKD[15], likely because factors such as diet and medication – major drivers of microbial variation in humans – are standardized or absent in our mouse model[16]. Functionally, bacterial metabolites are particularly relevant in kidney disease, as they can accumulate as a function of microbial production and insufficient renal excretion[5]. Thus, we performed plasma metabolomics by nuclear magnetic resonance (NMR), covering a large spectrum of metabolites (Fig.1b). Antibiotic depletion led to a substantial reduction of metabolite accumulation in STNx mice, with most pronounced changes in the aromatic region of the NMR spectrum (Fig.1c). We therefore quantified a targeted panel of aromatic metabolites in plasma by mass spectrometry (MS, Fig.1d). Bacterially derived toxins such as indoxyl sulfate (IxS), p-cresol sulfate and phenyl sulfate were significantly increased in STNx (Fig.1e) and consequently reduced by Abx treatment. Thus, kidney disease induces taxonomic alterations in the microbiome and elevates bacterial metabolite concentrations in the plasma that were abrogated by microbiome depletion.

To assess the impact of microbiome depletion on the degree of kidney dysfunction, we measured glomerular filtration rate (GFR) longitudinally. While both STNx groups displayed a comparable initial GFR reduction until week 8 (Fig.1f), Abx-treated STNx

121 mice preserved higher GFR at the endpoint (Fig.1g) despite similar remnant kidney
122 mass (Fig.S2a). Plasma cystatin C (CysC) confirmed this observation (Fig.S2b).
123 Focusing on cardiovascular comorbidities as the leading cause of mortality in CKD[6,17],
124 we next assessed cardiac and vascular damage. STNx induced cardiac remodeling
125 as reflected by increased heart weight, which was abolished by microbiome depletion
126 (Fig.1h). Longitudinal echocardiographic assessment of cardiac dimensions
127 corroborated this effect, becoming evident from week 8 onward (Fig.1i-k; Table S1)
128 despite similar GFR at this time point. While systolic function (ejection fraction, EF)
129 was preserved in all groups (Fig. 1l; Table S1), STNx mice displayed an increase in
130 E/e' (Fig.1i, m; Table S1) indicative of diastolic dysfunction, and a reduction in global
131 longitudinal strain (GLS, Fig.1n; Table S1), reflecting ventricular stiffening – both
132 rescued by microbiome depletion. Adverse cardiac remodeling is characterized by
133 cardiomyocyte hypertrophy, fibrosis and inflammation[18]. Interestingly, we observed a
134 comparable cardiomyocyte size in STNx (Fig.S2c-d), suggesting that the increased
135 heart weight is driven by extracellular matrix (ECM) deposition. Sirius red staining
136 revealed increased collagen deposition in STNx hearts, which was mitigated in
137 microbiome-depleted STNx mice (Fig.1o-p). In addition, STNx mice exhibited
138 increased cardiac leukocyte infiltration (Fig.1q), comprising mostly neutrophils and T
139 cells (Fig.S2e), which was ameliorated in Abx-treated STNx mice. In agreement,
140 plasma C-reactive protein (CRP) – a routine clinical marker of systemic inflammation
141 associated with cardiovascular risk[19] – was elevated in STNx mice and reduced by
142 Abx treatment (Fig.1r). These findings demonstrate that microbiome depletion
143 prevents hallmarks of adverse cardiac remodeling and diastolic dysfunction induced
144 by kidney disease.
145 Impaired kidney function typically leads to hypertension, a common cause for adverse
146 cardiac remodeling. Further evidence suggests that the gut microbiota influences
147 blood pressure (BP) and cardiac remodeling[20,21]. We therefore measured BP
148 longitudinally by radiotelemetry in both control and Abx-treated STNx mice (Fig.1s).
149 Both groups exhibited a similar increase in both systolic (SBP) and diastolic (DBP)
150 throughout the experiment, which was sustained towards the endpoint (Fig.1t-u, S2f-
151 i), suggesting that the cardioprotective effects observed in microbiota-depleted STNx
152 mice are independent of BP. To assess vascular function, we measured
153 vasorelaxation in isolated mesenteric arteries. Arteries from Abx-treated STNx mice
154 displayed an improved endothelium-dependent relaxation compared to those from

155 STNx mice (Fig.1v-w). Taken together, microbiome depletion protected mice with
156 reduced kidney function from further GFR loss, inflammation, cardiac and vascular
157 dysfunction despite a similar blood pressure increase, suggesting these benefits are
158 linked to immunological mechanisms.

159 **Microbiome-Dependent T_H17 Immunity and AhR Activation**

160 Since cardiac leukocyte influx was attenuated by microbiome depletion, we
161 hypothesized that microbiome-immune interactions are critical for the pathological
162 cardiac response to STNx. To assess immune cell composition, we performed flow
163 cytometry on splenic leukocytes (Fig.S3a). STNx induced an increased abundance of
164 neutrophils (Fig.2a) and a shift of T cells towards $CD4^+$ T helper subsets (Fig.2b), both
165 of which were prevented by Abx treatment. Flow cytometric analysis further revealed
166 an expansion of $CD44^+CD62L^-$ effector memory phenotypes (Fig.2c) for both $FoxP3^-$
167 conventional T helper cells (T_{conv}, Fig.2d) and $FoxP3^+$ regulatory T cells (T_{reg}, Fig.2e).
168 These alterations were abrogated in Abx-treated mice. Moreover, splenic T_{conv} from
169 STNx mice showed an increased abundance of RORγt$^+$ T_{conv} (T_H17, Fig.2f), which was
170 prevented by Abx. Similar patterns were detected in circulating and intestinal lamina
171 propria T cells (Fig.2g), indicating a microbiome-dependent T_H17-type inflammatory
172 response.

173 In parallel, we observed an expansion of RORγt$^+$ T_{reg}, hereafter referred to as $T_{reg}17$
174 cells (Fig.2h). While $T_{reg}17$ are known to limit inflammation in mucosal tissues[22], they
175 can also display T_H17-like effector functions, including IL-17A secretion[23]. To further
176 characterize $T_{reg}17$ in this inflammatory setting, we compared frequencies of PD-1$^+$,
177 CD69$^+$ and CD103$^+$ cells within the $T_{reg}17$ and T_{reg} compartment. $T_{reg}17$ cells showed
178 enrichment for these markers relative to total T_{reg} populations in Sham and Abx-treated
179 STNx mice; however, this pattern was not observed in STNx mice (Fig. S3b–d).
180 Additionally, IL-10$^+$ T_{reg} were reduced in STNx, but restored under Abx treatment
181 (Fig.S3e), altogether suggesting a loss of suppressive capacity favoring T_H17-like
182 effector functions. In line with these findings, STNx induced a sustained T_H17 and
183 $T_{reg}17$ increase over time (Fig.2i), while T_H17 of Sham and Abx did not show this
184 response. The parallel expansion of $T_{reg}17$ and T_H17 cells suggests ineffective
185 regulatory control and persistence of an inflammatory response.

186 Microbiota-derived metabolites can activate the aryl hydrocarbon receptor (AhR)[24],
187 which is known to modulate T cell function, including T_H17 differentiation[25,26].
188 Consistent with the observed increase in microbiome-derived tryptophan catabolites,
189 predominantly IxS, a known AhR ligand, plasma from STNx mice induced significantly
190 higher AhR activation in a cell-based reporter assay compared with Abx-treated and
191 Sham controls (Fig.2j). Moreover, *Cyp1a1*, a canonical AhR target gene, was
192 upregulated in splenic leukocytes from STNx mice compared to Abx-treated STNx
193 mice (Fig.2k), suggesting immune cells are affected by bacterial AhR ligands.

194 Next, we evaluated RORγt+ T cells in fibrotic hearts. We found an increase in $T_{reg}17$,
195 but not T_H17 cells, in whole hearts of STNx mice after 13 weeks (Fig.2l-m, Fig.S3f),
196 consistent with the observation that the cardiac microenvironment promotes T cell
197 transdifferentiation towards regulatory phenotypes[27]. Additionally, infiltrated
198 neutrophils were reduced in STNx mice treated with Abx (Fig.S3g). To further
199 characterize the inflammatory microenvironment of the heart, we performed bulk
200 mRNA sequencing from cardiac tissue. A substantial part of the STNx-associated
201 differentially expressed genes (DEG) were reversed by Abx treatment (Fig.2n).
202 Enrichment analysis on DEG identified Reactome pathways and Gene Ontology (GO)
203 terms involving tissue remodeling (e.g. fibronectin matrix formation, collagen
204 formation, extracellular matrix organization) and immunity (e.g. T cell receptor
205 signaling, interleukin 17 signaling, Fig.2o, S3h). Variation analysis of IL-17A-
206 associated gene sets revealed a significant increase in enrichment scores in STNx,
207 an effect normalized by Abx (Fig.2p). Taken together, our findings suggest that
208 microbiome-derived, AhR-activating metabolites drive a systemic T_H17-skewed
209 inflammatory response that impairs $T_{reg}17$ function and promotes adverse cardiac
210 remodeling in kidney disease.

211 **IxS exacerbates heart failure**

212 IxS has been shown to modulate T_H17 immunity in neuroinflammation[28]. *In vitro* T_H17
213 polarization of murine naïve CD4+ T cells was indeed stimulated dose-dependently by
214 IxS (Fig.3a-b). To test whether IxS stimulates a T_H17 response *in vivo* and aggravates
215 cardiac remodeling independent of advanced kidney dysfunction, we examined the
216 effects of IxS supplementation in a mouse model of heart failure with preserved
217 ejection fraction[29] (HFpEF, Fig.3c), the form of heart failure most frequently associated
218 with CKD[30]. We confirmed elevated IxS levels in mice exposed to IxS (Fig.3d),

219 although to a lesser extent compared to STNx mice and patients with CKD[31], likely
220 due to preserved renal clearance (Fig.3e). Still, IxS levels were sufficient to increase
221 splenic *Cyp1a1* expression (Fig.3f), but not liver *Cyp1a1* (Fig.S4a), indicating that the
222 immune system is particularly susceptible to AhR activation by bacterial metabolites.
223 Similar to STNx mice, splenic IL-17A$^+$ T_{conv} (Fig.3g), IL-17A$^+$ T_{reg} (Fig.3h) and
224 neutrophils (Fig.S4b) frequencies were elevated in response to IxS. IxS exposure
225 exacerbated heart failure, evidenced by increased heart weights (Fig.3i) and
226 pulmonary congestion (Fig.S4c). Echocardiography confirmed aggravation of diastolic
227 dysfunction (E/e', E/A, Fig.S4d-e; Table S2) with a preserved left ventricular EF
228 (Fig.S4f; Table S2). Next, we analyzed cardiac fibrosis, the most prominent feature of
229 STNx-associated cardiac remodeling. IxS-exposed hearts displayed higher collagen I
230 and fibronectin content, indicating increased interstitial cardiac fibrosis (Fig.3j-l). Thus,
231 IxS exacerbates heart failure and elicits a similar inflammatory response as observed
232 in experimental kidney disease.

233 **Cardiac fibroblasts respond to IL-17A and IxS to produce ECM**

234 In addition to the T cell-driven increase in IL-17A production, *Il17ra* expression was
235 upregulated in STNx hearts (Fig.4a), and likewise in IxS-treated HFpEF mice (Fig.4b).
236 To identify IL-17A-responsive cells among cardiac cells, we re-analyzed published
237 single nuclei RNA (sn-RNA) sequencing data from cardiac tissue of STNx and control
238 mice[32]. Among cardiac cell types, fibroblasts showed the highest *Il17ra* expression in
239 STNx (Fig.4c, Fig.S5a). Notably, fibroblasts also showed higher expression of AhR-
240 dependent genes (Fig.S5b) Interestingly, *Il17ra*$^+$ fibroblasts displayed higher ECM
241 gene set scores[33] than *Il17ra*$^-$ fibroblasts in STNx mice (Fig.4d). In line, the DEG were
242 characterized by a dominant representation of ECM components (Fig.S5c). To further
243 characterize *Il17ra*$^+$ fibroblast transcriptomes, we compared their DEG with different
244 fibroblast signatures known in both mouse and human cardiac tissue[34]. DEG were
245 enriched in myofibroblast-related and, to a lesser degree, cyclic and WNT-related
246 fibroblast-specific genes (Fig.4e), known for their pro-fibrotic and activated status.
247 Cytokine enrichment analysis revealed IL-17A as a prominent factor shaping DEG in
248 cardiac STNx lymphocytes (Fig.S5d). To test the response of cardiac fibroblasts to
249 AhR ligand IxS and IL-17A, respectively, we isolated fibroblasts from healthy murine
250 hearts (Fig.4f). Cell identity and purity were confirmed by immunocytochemistry and
251 flow cytometry (Fig.4g-h). As suggested by the sn-RNA data, IxS upregulated *Il17ra*

252 mRNA expression (Fig.4i), indicating IxS primes fibroblasts to sense IL-17A.
253 Consistent with this, coincubation with IL-17A and IxS resulted in a synergistic
254 increase in *Col1a1*, *Col1a2*, and *Acta2* expression (Fig.4j-l). In line with *in vivo* data,
255 IL17A downregulated *Abi3bp* expression, an ECM protein shown to be reduced in
256 heart failure[35] (Fig.4m). Immunocytochemistry confirmed the presence of COL1 and
257 IL17RA at the protein level (Fig.4n). Our data demonstrate that IL-17A signaling in
258 cardiac fibroblasts primed by IxS exposure leads to increased ECM production,
259 ultimately exacerbating cardiac fibrosis.

260 **AhR inhibition ameliorates cardiac remodeling in kidney disease**

261 Since STNx-associated cardiac remodeling occurs in an AhR-activating milieu that in
262 turn promotes IL-17A production and cardiac fibrosis, we investigated whether AhR
263 inhibition confers therapeutic benefit. For optimal translational potential, we re-
264 purposed the orally bioavailable AhR inhibitor BAY 2416964 (AhRi), currently under
265 investigation in solid malignancies[36]. *In vitro*, AhRi dose-dependently reduced the IxS-
266 induced upregulation of *Cyp1a1* expression in murine splenocytes (Fig.5a-b).
267 Furthermore, AhRi dose-dependently suppressed IxS-driven T_H17 polarization
268 (Fig.5a,c). In both assays, AhRi was effective at doses of $10^{-7.5}$-$10^{-6.5}$ M. Next, we
269 aimed to test the efficacy of AhRi *in vivo* in STNx mice (Fig.5d). Therefore, mice were
270 randomized based on serum CysC levels (Fig.S6a) to receive either AhRi or vehicle
271 starting two weeks after complete STNx through to week 13 by daily oral gavage.
272 Sham-operated vehicle-treated mice served as additional control. At the endpoint, we
273 detected similar levels of CysC in AhRi- and vehicle-treated mice (Fig.S6b). AhRi
274 treatment improved survival of STNx mice (Fig.5e) and lowered systemic
275 inflammation, as measured by plasma CRP (Fig.5f). Upregulation of canonical AhR
276 target gene *Cyp1a1* in immune cells was prevented by AhRi (Fig.5g), as well as the
277 STNx-associated increase in both T_H17 (Fig.5h) and $T_{reg}17$(Fig.5i). In line, IL-17A+
278 T_{conv} and T_{reg} were reduced by AhRi (Fig.S6c-d). We observed an improvement of the
279 cardiac phenotype upon AhRi reminiscent of the Abx effect, with lower left ventricular
280 mass (Fig.5j), and improved cardiac function (Fig.5k-l, Table S3) and fibrosis (Fig.5m-
281 n), together with lower cardiac *Il17ra* expression (Fig.5o). Bulk transcriptomic analyzes
282 of cardiac tissue showed similar effects as observed with Abx treatment, with a
283 reduction in GO terms and pathways involved in ECM formation and inflammatory
284 processes (Fig.5p, Fig.S6e). Targeted analysis of T_H17-related signaling pathways

285 revealed significantly higher scores upon STNx, which were rescued by AhRi (Fig.5q).
286 These findings identify the AhR as a key mediator of inflammation and cardiac
287 remodeling in kidney disease and suggest AhRi as a therapeutic strategy.

288 **Conserved pro-fibrotic IxS-AhR-T_H17 axis in patients with CKD**

289 We further aimed to explore the translational potential of AhRi by investigating the
290 efficacy in human cells. AhRi dose-dependently blocked the IxS-stimulated AhR
291 activity in human AhR reporter cells (Fig.6a). Likewise, AhRi reduced AhR activity of
292 serum collected from patients with kidney failure requiring hemodialysis (HD) to levels
293 observed with serum from healthy donors (HC, Fig.6b-c; Table S4). Moreover, addition
294 of HD serum to human T_H17 polarization assays increased T_H17 cells compared to
295 HC (Fig.6b,d). Hence, the kidney disease-responsive AhR-T_H17 axis identified in mice
296 is conserved in humans.
297 Next, we analyzed plasma IL-17A levels in patients with CKD and healthy controls
298 from the UK Biobank (Table S5). Circulating IL-17A concentrations increased
299 progressively with worsening kidney function (Fig.6e, n= 15 120 with available eGFR
300 and albuminuria). IL-17A concentrations were further elevated in patients with eGFR
301 below 60 (CKD) and HFpEF (n = 5 497) compared to patients with only CKD
302 (n = 15 981, Fig.6f). Furthermore, higher plasma IL-17A in individuals with CKD
303 (n = 2 785) was associated with all-cause mortality, even after adjustment for
304 conventional risk factors (Fig.6g-h). These findings substantiate kidney disease-
305 dependent IL-17A response at population scale.
306 To verify the role of AhR signaling and IL-17A in fibroblast activation in humans, we
307 used publicly available single cell RNA (sc-RNA) sequencing data. Since cardiac sc-
308 RNA data from patients with CKD were not available, we explored data from kidney
309 tissue of patients with CKD and healthy controls[37]. Fibroblasts of patients with CKD
310 displayed the highest AhR enrichment scores compared to other kidney cell types
311 (Fig.S7a). Moreover, myofibroblasts expressed the highest levels of *IL17RA* (Fig.S7b),
312 and *IL17RA* expressing myofibroblasts exhibited markedly higher ECM module scores
313 (Fig.S7c). In line, pro-fibrotic and ECM-associated genes were among the major DEG
314 (Fig.S7d), indicating that IL-17A-responsive fibroblasts represent a pro-fibrotic subset.

315 Next, we stimulated primary human cardiac fibroblasts with serum from hemodialysis
316 patients (HD) or healthy controls (HC) (Fig.6i). HD serum induced upregulation of
317 *IL17RA* (Fig.6j, Fig.S8a) together with ECM-associated transcripts such as *COL1A2*

318 and *ACTA2* (Fig.6k-m, Fig.S8b-d). We tested whether these effects could be
319 prevented by AhRi or secukinumab, a human monoclonal antibody used in clinical
320 routine targeting IL-17A (αIL-17A). Both AhRi and αIL-17A mitigated the pro-fibrotic
321 effects (Fig.6k-m, Fig.S8b-d). However, only AhRi reduced *IL-17RA* expression
322 (Fig.6j, Fig.S8a). Similar to murine cardiac fibroblasts, IxS upregulated *IL17RA*
323 expression in primary human cardiac fibroblasts, an effect abrogated by AhRi
324 (Fig.S8e). Both IxS and IL-17A increased *COL1A2* and *ACTA2* expression, whereas
325 co-stimulation with both ligands again had a synergistic effect, leading to the highest
326 pro-fibrotic transcriptional response (Fig.S8f-h). Proliferation was not altered with IL-
327 17A and IxS co-incubation, as determined by Ki-67 staining (Fig.S8i-j). Taken
328 together, translation of our findings to patients with CKD using data from UK Biobank,
329 human sc-RNA sequencing and *in vitro* assays using patient-derived serum show a
330 conserved pro-fibrotic IxS-AhR-T_H17 axis.

Discussion

This study demonstrates that kidney disease recalibrates microbiome-host interactions to potentiate inflammation-mediated cardiac fibrosis. We identify a microbial AhR-activating metabolite driving a pathogenic T_H17 response that engages IL-17A-responsive cardiac fibroblasts, positioning the metabolite-AhR-IL-17A axis as a therapeutic target to prevent cardiac fibrosis in kidney disease.

Inflammation is a key driver of CVD. In CKD, inflammation is substantially elevated, paralleling a markedly increased risk for CVD[38]. Evidence suggests that CVD development in CKD extends beyond traditional risk factors[39] such as hypertension, hyperlipidemia, and diabetes, yet underlying mechanisms remain less characterized. Adverse cardiac remodeling and fibrosis are prevalent in CKD[40], with heart failure representing a frequent clinical manifestation[41]. The microbiome plays a central role in immune modulation, in part via action of bacterial metabolites. In CKD, these metabolites accumulate and contribute to a pro-inflammatory internal milieu. Such metabolites were shown to be of bacterial colonic origin and can reach toxic levels in CKD[5]. To date, therapeutic strategies aimed at improving outcomes by reducing bacterial metabolite levels through unspecific intestinal adsorption showed limited success[42], underscoring the need for a refined understanding of microbiome-host interaction in CKD.

Our mechanistic investigations were prompted by the observation that the depletion of the gut microbiome in a state of reduced kidney function drastically reduced the development of cardiac fibrosis as well as diastolic dysfunction, and suppressed systemic inflammation, as evidenced by a lower plasma CRP. Remarkably, cardioprotection occurred despite persistently high blood pressure, in line with a clinical observation showing that cardiac fibrosis in CKD occurs independent of hypertension[40], which has so far not been linked to the gut microbiome. The profound inflammation encouraged us to investigate cellular immunity further, in which a microbiome-dependent T_H17 response to STNx became evident. While IL-17A has previously been associated to ischemic heart disease[43] and kidney disease progression after acute kidney injury[44], it has not been highlighted as a cytokine linking heart disease and CKD. Our analyzes of UK Biobank data suggest that this may indeed be the case, demonstrating elevated IL-17A levels in patients with CKD and

363 HFpEF. IL-17A plasma concentrations increased in a CKD stage-dependent manner
364 and were associated with excess mortality.
365 We previously hypothesized that CKD-linked inflammation is mediated by the AhR[26].
366 Plasma AhR activation potential increased following STNx, with splenocytes exhibiting
367 AhR-dependent gene expression; both effects were abrogated by microbiome
368 depletion. We present evidence that AhR activation and T_H17 response are mediated
369 via the AhR by increased levels of IxS, a known microbiome-derived AhR-activating
370 ligand. *In vitro*, IxS induced T_H17 polarization dose-dependently. *In vivo*, oral
371 administration of IxS in an experimental heart failure model increased AhR activation
372 and AhR-dependent gene expression in immune cells, promoted T_H17 expansion, and
373 aggravated cardiac fibrosis, despite preserved kidney function. Further *in vivo*
374 evidence is provided by AhR inhibition in STNx mice, which abrogated AhR-dependent
375 gene expression in immune cells, T_H17 expansion and systemic inflammation, as well
376 as cardiac fibrosis and diastolic dysfunction. Thus, IxS-dependent AhR activation
377 appears to be central to cardiac remodeling in kidney disease.
378 As an environmental sensor integrating various external and endogenous cues, the
379 AhR is known to regulate T_H17 differentiation[45]. AhR-deficient naïve T cells exhibit
380 reduced differentiation[45], while AhR activation by high affinity ligands has been shown
381 to promote T_H17 and autoimmune disease[46]. However, AhR-mediated effects on T_H17
382 differentiation depend on the ligand and cytokine milieu[47]. IxS is a known endogenous
383 AhR ligand[28] and has been linked with inflammatory milieus[48] as well as T_H17-
384 mediated autoimmunity[28]. We present evidence that IxS activates AhR transcriptional
385 programs in CD4+ cells to promote a pathogenic T_H17 response in kidney disease.
386 We show that IxS drives RORγt expression and IL-17A production in CD4+ T cells *in*
387 *vitro* and *in vivo*. Intriguingly, we also detected increased IL-17A production by Foxp3+
388 CD4+ T_{reg}, as well as increased RORγt expression in CD4+ FoxP3+ cells ($T_{reg}17$),
389 especially in cardiac tissue. While $T_{reg}17$ cells typically restrain IL-17A-driven
390 inflammation through IL-10[48], their regulatory capacity appears diminished in the
391 present uremic setting, where IL-17A-mediated inflammation is less effectively
392 controlled. Consistently, $T_{reg}17$ cells from uremic STNx mice exhibited reduced
393 expression of PD-1, CD103, and CD69 – proteins implicated in the maintenance of
394 suppressive function[49-51] – compared with microbiome-depleted and kidney-healthy
395 controls. This phenotype suggests a functional shift in $T_{reg}17$ cells toward RORγt-
396 driven effector activity at the expense of FoxP3-dependent regulatory functions.

397 Moreover, IL-10 production was lowest in T_{reg}s from STNx mice. The STNx-induced
398 IL-17A response was accompanied by neutrophilia and enhanced cardiac neutrophil
399 infiltration. IL-17A is a known regulator of neutrophils, promoting granulopoiesis and
400 inducing neutrophil-attracting chemokines in stromal and cardiac cells[52]. Circulating
401 neutrophils correlate with IL-17A levels[53]. Once recruited, neutrophils maintain IL-17A-
402 driven inflammation through release of inflammatory mediators, including IL-1β and
403 neutrophil extracellular traps[54]. Together, these findings reveal a microbiome-
404 dependent, AhR-mediated and IL-17A-driven inflammatory program in kidney disease.
405 This study identifies cardiac fibroblasts as key targets of IL-17A, characterized by
406 enhanced IL-17RA expression *in vivo*, which in turn drives ECM production and
407 promotes cardiac fibrosis. It has been reported that IL-17A enhances fibroblast
408 proliferation and migration[55] and induces a proinflammatory fibroblast phenotype
409 involving GM-CSF[56]. We demonstrate that IxS effectively primes cardiac fibroblasts
410 via AhR-dependent upregulation of IL-17RA in murine and human cells, suggesting
411 that the same bacterial metabolite that drives IL-17A-mediated inflammation also
412 sensitizes fibroblasts to IL-17A signaling and ECM production. Thus, IxS orchestrates
413 inflammation and tissue remodeling through AhR signaling, providing a mechanistic
414 explanation for the pronounced cardiac fibrosis observed in CKD and a strong
415 rationale for AhR inhibition as a therapeutic strategy. Notably, pharmacological AhR
416 targeting with a small-molecule inhibitor currently under clinical investigation for cancer
417 treatment[36] (NCT04999202) proved effective both *in vivo* in STNx mice and *in vitro* in
418 human cardiac fibroblasts, highlighting its translational potential. Targeting host
419 sensing of uremic toxins may uncouple disease-driving microbiome-derived
420 metabolites from downstream inflammatory responses. Integrating AhR inhibition with
421 existing therapies could therefore provide a complementary strategy to mitigate
422 adverse cardiovascular comorbidities in CKD.
423 Taken together, our findings identify an IxS-AhR-IL-17A axis as a central driver of
424 cardiac inflammation and fibrosis in kidney disease. We demonstrate how kidney
425 dysfunction promotes cardiac pathology through specific microbiome-derived
426 metabolites. Our study positions IxS not merely as a biomarker of uremia but as an
427 active pathogenic effector linking microbial metabolite accumulation to maladaptive
428 immunity and tissue fibrosis via AhR signaling. AhR inhibition may offer a means to
429 selectively target uremic downstream signaling while preserving potentially beneficial

430 microbiome functions. More broadly, these findings refine our understanding of
431 disease-to-multimorbidity transition in chronic kidney disease.

Methods

Animal studies

All experiments were performed in accordance with the German/European law for animal protection. Experimental protocols were approved by the local ethic authorities under the G0190/21 and G0019/21 licenses. For all *in vivo* experiments, male 129/Sv mice (wild type [WT]; strain 129S2/SvPasOrlRj) were obtained from Janvier Labs, France, and housed at 12-hour day:night cycle with free access to water and food (Chow diet, Ssniff, V1124-300) in the Preclinical Research Center (PRC) of the Max-Delbrück-Center for Molecular Medicine (MDC). Mice were habituated for 2 weeks before use. Individual mice served as experimental units, and all animals within a cage received the same treatment.

For the Abx trial, mice were distributed according to body weight (BW) to four groups prior to treatment (STNx ± Abx and Sham ± Abx). The Abx experiment consisted of two independent cohorts. A longitudinal cohort was designed to evaluate dynamics in kidney function, metabolomics and immunity in STNx groups (n=11 per group) and Shams (n=7 per group) across timepoints (w1, w3, w8, w13). Each timepoint had its own independent cohort to collect biomaterial. A second cohort was designed for terminal assessments, focused on organ damage and tissue level responses in STNx groups (n=12) and Shams (n=7). Both cohorts were exploratory, thereby no prior sample size calculation was performed. Endpoint analyzes were performed combining both cohorts if applicable. Animals were excluded in cases of surgical failure or failure to reach minimum kidney function thresholds. Animals were sacrificed during the course of the study if BW dropped under 20% or they showed clear signs of pain or discomfort. The longitudinal cohort resulted in: w1 - Sham n=7; Abx n=6; STNx n= 6; STNx Abx n= 6. w3 - Sham n=6; Abx n= 7; STNx n=10; STNx Abx n=7. w8 - Sham n=5; Abx n=5; STNx n=6; STNx Abx n=6. w13 - Sham n=6; Abx n=4; STNx n=6; STNx Abx n=6. The endpoint cohort resulted in: Sham n=7; Abx n=7; STNx n=11; STNx Abx n=10.

For the HFD/L-NAME trial, mice were assigned according to BW and cage to receive either potassium indoxyl sulfate (IxS) exposure (n=16) or control (KCl; n=16) over the drinking water *ad libitum.* Sample size was calculated using G Power according to a partial effect size of the alleviation of the STNx-induced diastolic dysfunction by Abx.

464 During the experiments n=3 from the control group were taken out of the experiment
465 due to prespecified criteria.

466 For the AhRi trial, mice underwent STNx (n=24) or Sham (n=6) surgery. Sample size
467 was calculated using G Power according to the effect size of the alleviation of the
468 STNx-induced cardiac fibrosis by Abx. The same exclusion criteria were followed as
469 in the Abx trial. To ensure equal kidney dysfunction before treatment, mice were
470 equally distributed into 2 groups according to BW and plasma CysC two weeks after
471 completed STNx surgery, and assigned to receive either AhRi (n=10) or vehicle (n=9).
472 During the experiments n=4 vehicle and n=2 AhRi-treated animals were taken out of
473 the experiment due to prespecified criteria and analyzed at an earlier time point.

474 Across all experiments, blinding during *in vivo* procedures was not possible due to
475 model-specific features; however, all outcome measurements and data analysis were
476 performed blindly.

477 Subtotal nephrectomy

478 Mice between 10 and 12 weeks old were anaesthetized with isoflurane (2.5%
479 isoflurane-air) and subjected to subtotal nephrectomy operation (STNx). Briefly, the
480 left kidney was exposed, and the lower and upper poles were excised using a
481 cauterizer (Surtron 160, LED SpA). The adrenal gland was separated from the kidney
482 to preserve its function. 2 weeks later, a total nephrectomy of the right kidney was
483 performed. Sham-operated mice underwent a simple flank incision and sutures. All
484 animals received pre-emptive buprenorphine (30 mg/kg, intraperitoneal (i.p.) injection)
485 30 min before surgery. Post surgery, analgesia consisted of metamizole (800
486 mg/kg/24h) administered over the drinking water for 3 days.

487 Antibiotic treatment

488 Mice were given an antibiotic cocktail (all obtained individually from Thermofisher)
489 containing ampicillin (0.5 g/L), vancomycin hydrochloride (0.5 g/L), neomycin sulfate
490 (1 g/L) and metronidazole (1 g/L) in the drinking water throughout the entire study
491 period. 1% glucose was added into the mixture for organoleptic purposes. Control
492 animals received only glucose in the drinking water. Treatment was started one week
493 prior to the first operation and antibiotics were refreshed every 3 days.

494 AhR inhibitor treatment

495 Mice were stratified and randomized as described above to receive either small-
496 molecule AhR inhibitor BAY2416964 (GlpBio) or vehicle, starting two weeks after
497 completed STNx surgery. AhRi was formulated in a mixture of water, Solutol® HS 15
498 (polyethylene glycol 12-hydroxystearate; Merck) and ethanol at a 50:40:10 ratio
499 (v/v)[36]. The vehicle control consisted of the solvent mixture alone. A daily AhRi dose
500 of 30 mg/kg was selected based on a previously reported safe and effective regimen[36].

501 HFpEF model

502 12-week-old mice were switched to a high fat diet (HFD; 60% kcal fat, Research diets,
503 D19032801-1.5V) and administered Nω-nitro-L-arginine methyl ester hydrochloride
504 (L-NAME; 1 g/L, Merck) in the drinking water for 15 weeks. Mice received either
505 potassium indoxyl sulfate (IxS; 1 g/L, Merck) or equimolar potassium chloride (KCl;
506 0.3 g/L, Merck) in the drinking water throughout the study. This model has been
507 published previously[29].

508

509 **Microbiome**

510 Cecal DNA isolation

511 At different timepoints (w1, w3, w8, w13), cecal contents were collected at the time of
512 euthanasia. Samples were immediately fresh-frozen on dry ice and kept at -80 °C.
513 DNA was isolated from cecal samples using the Quick-DNA Miniprep Kit (Zymo
514 Research) according to manufacturer's protocol. Absolute bacterial load was
515 determined by qPCR for the *16S* gene using SYBR Green as described below.

516 Microbiome analysis

517 Samples were stored at -20°C and sent for 16S rRNA gene amplicon sequencing
518 (Novogene, Cambridge, UK). The V3-V4 hypervariable region of the 16S rRNA gene
519 was amplified using universal primers 341F (5′-CCTAYGGGRBGCASCAG-3′) and
520 806R (5′-GGACTACNNGGGTATCTAAT-3′), which were appended with sample-
521 specific barcodes and Illumina sequencing adapters. Amplicons were purified using
522 AMPure XP magnetic beads and quantified for library preparation.

523 Libraries were constructed using the NEBNext® Ultra™ II DNA Library Prep Kit and
524 sequenced on an Illumina NovaSeq 6000 platform (paired-end 2×250 bp), targeting

525 approximately 30,000 raw reads per sample. Annotation was performed in R (v4.0.3).
526 Demultiplexed reads were processed through DADA2 pipeline (v1.25.2) and
527 taxonomic assignment was based on the rRNA database SILVA (v138.1) with a 80%
528 boodstrapped confidence. Only ASVs that were present in at least 20% of the samples
529 were considered for further downstream analysis.

530

531 **Nuclear magnetic resonance (NMR) spectroscopy**

532 Sample preparation

533 Plasma samples were prepared using 3 mm SampleJet NMR tubes. 100 µL of plasma
534 was mixed thoroughly with 78 µL of 0.1 mol/L phosphate buffer (pH 7.4) and 19.5 µL
535 of a 0.75% (w) solution of 3-trimethylsilyl-2,2,3,3-tetradeuteropropionate (TSP; Sigma-
536 Aldrich, Taufkirchen, Germany) in deuterium oxide, serving as an internal standard for
537 NMR measurements. As an additional internal standard 2.5 µL of formic acid (240
538 mM) was added. Prepared samples were measured as described below.

539 Data acquisition

540 All NMR experiments were performed on a 600 MHz Bruker Avance III HD
541 spectrometer, using a triple resonance (^{1}H, ^{13}C, ^{15}N, ^{2}H lock) helium cooled cryoprobe
542 with z-gradient. Samples were handled by an automatic Bruker SampleJet sample
543 changer (Bruker Biospin GmbH, Ettlingen, Germany). Tuning and matching of the
544 probe as well as locking and shimming of the sample were performed automatically.
545 For each sample one dimensional ^{1}H NMR spectra were obtained at 310 K using Carr-
546 Purcell-Meiboom-Gill (CPMG) pulse sequence. For each spectrum, 512 scans were
547 collected into 72k datapoints over a spectral width of 12019 Hz. An acquisition time
548 and T_1 relaxation delay of 3.07 and 4 seconds per scan were used, respectively. All
549 NMR spectra were processed with TopSpin 4.5.0. Free induction decays (FIDs) were
550 Fourier transformed, phase corrected and subjected to exponential line broadening
551 function of 0.3 Hz. All the chemical shifts were manually referenced to formic acid at
552 8.46 ppm.

553 To compensate for chemical shifts perturbations bucket tables were generated from
554 the processed 1D CPMG spectra using AMIX software (version 3.9.13, Bruker,
555 Ettlingen, Germany). The spectra over a range from δ0.11 to δ 9.5 ppm were divided

556 into the buckets at an equal width of 0.01 ppm with the regions at δ4.59 - δ4.77 ppm
557 being excluded as the water peak. The spectra were not normalized.

558 Bucket analysis

559 Only buckets within the aromatic region (6.75-8.00 ppm) were retained for subsequent
560 analyzes. For each treatment background, sham animals were used to calculate the
561 mean intensity for every aromatic bucket, providing treatment-matched reference
562 values. Each STNx (± Abx) sample was then compared with its corresponding sham
563 reference by determining, for each bucket, whether its intensity exceeded the sham
564 mean. The proportion and number of aromatic buckets classified as increased were
565 calculated per sample and statistically compared between groups using Mann Whitney
566 U test.

567

568 **Liquid chromatography-mass spectrometry**

569 Tryptophan panel

570 Tryptophan and its downstream metabolites were quantified in serum and plasma
571 samples. If not stated otherwise, the sample preparation was applied as stated
572 previously[57]. Briefly, 10 µL of an aqueous stable-isotope labelled internal standard
573 mixture was added to 50 µL of serum/ plasma. For protein precipitation samples were
574 diluted in a ratio of 1:5 with 100% cold methanol, vortexed, and stored at -80 °C for
575 24 h. Samples were centrifugated at 10,000×g at 4 °C for 5 min. The supernatant was
576 collected. The protein pellet was washed twice by addition of 200 µL of cold 80%
577 MeOH and subsequent centrifugation at 10,000×g (washing step 1) and 12,000×g
578 (washing step 2) at 4 °C for 5 min. For each sample, all supernatants were combined
579 and dried using a vacuum evaporator (CombiDancer, Hettich AG, Bäch, Switzerland).
580 All samples were reconstituted in 100 µL in water.

581 An ExionLC-30AD HPLC system (AB Sciex, Germany, Darmstadt) was used for the
582 chromatographic separation of metabolites on an ACQUITY Premier HSS T3, 1.8 µm,
583 2.1 × 150 mm reversed-phase column (Waters, Eschborn, Germany) reversed-phase
584 column. Gradient elution was performed with mobile phase A consisting of 0.1% formic
585 acid in water and mobile phase B of 0.1% formic acid in acetonitrile. Metabolite
586 detection was performed with a TripleQuad6500^{+} (AB Sciex, Germany, Darmstadt)
587 performing positive/ negative-switching for the ionization. Peak integration and data

evaluation were carried out using SciexOS-MQ Software (Version 2.1.6, AB Sciex, Germany, Darmstadt). Results were normalized to sample volumes.

3-Indoxyl sulfate quantification

For the HFD/L-NAME trial, frozen plasma samples were thawed at RT and then 70 µL of each sample was mixed with 210 µL of a cold methanolic solution of the internal standard d_5-IxS (Toronto Research Chemicals, Toronto, Canada), concentrated to 1 µmol/L . Proteins were precipitated by vortexing for 1 min and subsequent storage for 60 min at -20°C. Supernatants were obtained by centrifugation at 9,400 g at 4°C for 10 min and subjected to LC-MS/MS IxS quantification applying the multiple reaction monitoring (MRM) method. Chromatographic separation was achieved on a 1290 Infinity II HPLC (Agilent Technologies, Waldbronn, Germany) equipped with a Poroshell 120 EC-C18 column (3.0 x 150 mm, 2.7 µm; Agilent Technologies) guarded by a pre-column (3.0 x 5 mm, 2.7 µm) of identical material. Water (eluent A) and acetonitrile (eluent B), both acidified with 0.1% formic acid, were pumped with 0.4 mL/min. Elution of IxS and its internal standard was achieved with a 10-min linear gradient from 5% to 90% eluent B. Total run-time was 16 min including re-equilibration of the LC system. MS/MS analyzes were carried out using an Ultivo (6465B) triple-quadrupole mass spectrometer (Agilent Technologies) operating in the negative electrospray ionization mode (ESI-). The following ion source parameters were set: sheath gas temperature, 400°C; sheath gas flow, 12 l/min of nitrogen; nebulizer pressure, 50 psi; drying gas temperature, 100°C; drying gas flow, 9 l/min of nitrogen; capillary voltage, 2.0 kV; nozzle voltage, 0.4 kV. The following mass transitions were recorded (fragmentor voltage [FV] and collision energies [CE] in parentheses): IxS: *m/z* 212.0 → 79.8 (FV: 102 V, CE: 28 eV, quantifier), *m/z* 212.0 → 80.9 (FV: 102 V, CE: 16 eV), *m/z* 212.0 → 131.9 (FV: 102 V, CE: 20 eV), d_5-IxS: *m/z* 217.0 → 79.8 (FV: 82 V, CE: 28 eV, quantifier), *m/z* 217.0 → 80.9 (FV: 82 V, CE: 16 eV), *m/z* 217.0 → 137.0 (FV: 82 V, CE: 20 eV). Peak areas were determined with MassHunter Quantitative Analysis software (version 10.1, Agilent Technologies) and IxS was directly quantified via its internal standard d_5-IxS that was concentrated to 750 nmol/L in the samples.

618 **Transdermal measurement of glomerular filtration rate**

619 FITC-sinistrin was reconstituted with PBS (40 mg/mL) and stored at -20 °C. Mice were
620 anaesthetized with isoflurane and prone-placed on a heat pad. After shaving, the GFR
621 monitor was attached on the right side of the back below the ribs. The measurement
622 was recorded for 2-3 minutes prior to intravenous FITC-sinistrin injection (60 mg/kg)
623 via either the tail vein or retro-orbital injection to set a steady baseline. Mice were then
624 allowed to recover from anesthesia for the measurement of FITC decay (1-2 hours).
625 Transcutaneous GFR was calculated from FITC-sinistrin half-time using a 3-
626 compartment model (MBLab2, Medibeacon).

627

628 **Clinical chemistry**

629 Clinical parameters (plasma CRP, Cystatin C) were analyzed using an AU480 clinical
630 chemistry analyzer (Beckman Coulter).

631

632 **Echocardiography**

633 Echocardiography was performed according to a standard operation protocol[58].
634 Briefly, mice were examined on a Vevo 3100 Imaging System equipped with a 30 MHz
635 linear transducer (MX400; FUJIFILM VisualSonics Inc., Canada). Anaesthesia was
636 induced by 3% isoflurane (in 80% oxygen). For image acquisition, isoflurane
637 concentration was reduced to 1-1.5%, and adjusted to maintain comparable heart
638 rates. All images were analyzed using Vevo LAB analysis software (FUJIFILM
639 VisualSonics Inc.). Systolic function and cardiac dimensions were assessed using B-
640 mode and M-mode echocardiography obtained from the parasternal long-axis view
641 and the parasternal short-axis view at the mid-papillary level. Diastolic function was
642 evaluated using conventional pulsed-wave Doppler to measure transmitral flow in the
643 apical four-chamber view. Tissue Doppler recordings from the septal mitral annulus
644 were used to assess myocardial relaxation velocity. The following parameters were
645 analyzed: E/A (early diastolic filling velocity to atrial contraction), E/e′ (early filling
646 velocity to early diastolic annular motion), and IVRT (isovolumetric relaxation time).
647 Strain and M-mode measurements were derived from three images per parameter,
648 with three cardiac cycles per image, and subsequently averaged. Diastolic Doppler
649 measurements were obtained from three independent images, each with three

650 repeated measurements. Speckle-tracking analysis was performed using parasternal
651 long-axis and short-axis images, with epicardial and endocardial contours used to
652 quantify longitudinal, circumferential, and radial deformation[59]. Echocardiographic
653 parameters for each trial are summarized in Tables S1–S3.

654

655 **Cardiac histology**

656 Hearts were immediately collected after sacrifice. Cardiac tips were snap-frozen at
657 -80 °C for RNA isolation. The remaining tissue was either fixed in 10% neutral buffered
658 formalin solution (Merck) for 36 h at room temperature (RT) and then switched to 1%
659 until further use, or fixed in 4% paraformaldehyde (PFA) in PBS for 5 h at 4 °C.

660 For Picrosirius Red staining (PSR), formalin-fixed heart tissues were embedded in
661 paraffin and transversally sectioned (2 µm) using an HM 340E Rotary Microtome
662 (Epredia). Prior to staining with PSR, tissue sections were deparaffinated, rehydrated,
663 washed and incubated in PSR working solution (Morphisto) according to
664 manufacturer's protocol, with the exception of using ROTIClear (Carl Roth) as a xylol
665 substitute. After washing and dehydration, samples were mounted in water-free
666 medium (ROTIMount, Carl Roth, HP68.1).

667 For IHC stainings, PFA-fixed cardiac tissue was washed in PBS and incubated in 15%
668 sucrose in PBS for 6-12h and 30% sucrose for 6-12h under constant rotation at 4°C
669 for cryoprotection. Cardiac tissue was frozen embedded in Tissue-Tek O.C.T.
670 Compound (Sakura Finetek) in -40°C methyl butane and stored at -80% until further
671 use. Hearts were cut into 7 µm cryosections on a Cryostat Microtome (CMC3050 S,
672 Leica Biosystems). Prior to staining, cryosections were re-hydrated in Tris-buffered
673 saline (TBS) for 10 min at RT and subsequently permeabilized in TBS with 0.1%
674 Tween 20 (TBST) for 5 min at RT. Blocking was performed with 5% bovine serum
675 albumin (BSA) and 10% normal donkey serum (NDS) in TBST for 20 min at RT.

676 For wheat germ agglutinin (WGA) staining, cryosections were incubated with WGA
677 Fluorescein (1:800, Vector Laboratories) and DAPI staining solution (1:1000, Biotium)
678 in TBST + 5% NDS for 2 h at RT. For extracellular matrix (ECM) protein staining,
679 cryosections were incubated with primary antibodies, rabbit anti-fibronectin (1:100,
680 polyclonal, abcam) and goat anti-type I collagen (1:50, polyclonal, Southern Biotech),
681 in TBST + 5% NDS overnight at 4 °C. After washing in TBST, cryosections were

682 incubated with secondary antibodies, donkey anti-rabbit IgG Alexa Fluor Plus 488
683 (1:1000, Thermo Fisher) and anti-goat IgG Alexa Fluor Plus 555 (1:1000, Thermo
684 Fisher), together with DAPI (1:1000, Biotium) in TBST + 5% NDS for 1 h at RT. After
685 washing in TBS, slides were mounted with DAKO fluorescent mounting medium.

686 Slides were imaged using the PANNORAMIC™ MIDI II digital slide scanner
687 (3DHistech) with a 20x objective. For each heart, six representative snapshots were
688 taken at 20x magnification using CaseViewer (v2.2.1, 3DHistech) for downstream
689 analysis.

690 For PSR and ECM stainings, the percentage of positively stained area was quantified.
691 Snapshots were pre-processed using Fiji to generate a binary image of stained versus
692 unstained areas, and quantification was performed using CellProfiler. For WGA
693 staining, the size of the unstained area was quantified. After pre-processing in Fiji,
694 each snapshot was segmented in Ilastik by classifying pixels as stained or unstained
695 using an interactive machine-learning algorithm. The size of segmented objects
696 (unstained areas) was subsequently quantified using CellProfiler. The mean value
697 across all snapshots was calculated per animal.

698

699 **Telemetry**

700 In a subset of mice (n= 7 STNx, n= 7 STNx Abx) subcutaneous radiotelemetry
701 transmitters (PA-C10 BP, DSI data science international, St. Paul, MN, USA) were
702 implanted one week prior to the administration of antibiotics. Due to the length of the
703 study, we measured blood pressure on a weekly 3-day period (except w2, which had
704 a 2-day measurement). Means and SD per each 3-day measurement period were
705 calculated and values with an absolute SD > 5 were excluded from downstream
706 analysis. Longitudinal curves were generated by a non-parametric, locally weighted
707 scatterplot smoothing (LOESS) regression. For statistical analysis, systolic and
708 diastolic blood pressure AUCs were computed and divided by the total elapsed
709 recording time (in minutes) to yield average blood pressure per minute. Group
710 differences were assessed using a Wilcoxon test. Of the 14 mice initially implanted
711 with radiotelemetry transmitters, 5 mice died perioperatively and were excluded. An
712 additional 3 mice were removed prior to analysis due to telemetry signal instability and
713 inconsistent blood pressure recordings. Thus, only animals that survived surgery and

714 maintained stable telemetry signals throughout the study (n=3 per group) were
715 included in the final analysis.

716

717 **Wire myography**

718 From a subset of animals (n=5 STNx, n=8 STNx + Abx), mesenteric arteries were
719 removed, immediately transferred to cold (4°C) oxygenated (95% O_2/ 5% CO_2)
720 physiological salt solution (PSS: 119 NaCl, 4.7 KCl, 1.2 KH_2PO_4, 25 $NaHCO_3$, 1.2
721 Mg_2SO_4, 11.1 glucose, and 1.6 $CaCl_2$ in mmol/L), and dissected into 2-mm rings (n=2
722 per animal). Perivascular fat and connective tissues were removed. Each ring was
723 positioned between two stainless steel wires (0.0394-mm dia.) in a 5-mL PSS-filled
724 organ bath of Small Vessel Myograph (DMT 630MA, Danish Myo Technology, Aarhus,
725 Denmark). The PSS was continuously oxygenated and kept at 37°C (pH 7.4).
726 Mesenteric rings were placed under a tension equivalent to that generated at 0.9 times
727 the diameter of the vessel at 100 mm Hg. This normalization procedure was performed
728 to obtain the passive diameter of the vessel at 100 mm Hg. The software LabChart 8
729 was used for data acquisition and display. The rings were precontracted with the KCl
730 buffer (119 NaCl, 60 KCl, 1.2 KH_2PO_4, 25 $NaHCO_3$, 1.2 Mg_2SO_4, 11.1 glucose, and
731 1.6 $CaCl_2$ in mmol/L) and equilibrated until a stable resting tension was acquired. To
732 test the endothelial function, vessels were precontracted with 1 µmol/L phenylephrine.
733 After all vessel segments had reached a stable contraction plateau, increasing doses
734 of acetylcholine were administered to the organ baths (3 to 1000 nmol/L). Tension is
735 expressed as a percentage of the steady-state tension (100%) obtained with
736 phenylephrine.

737

738 **Immunophenotyping**

739 <u>Plasma collection, immune cell isolation and flow cytometry measurements</u>

740 Whole blood was collected in lithium-heparin syringes (80 IU/3 mL, BD Vacutainer A-
741 Line) for anticoagulation and centrifuged at 1,500 g for 15 min at RT. Plasma was
742 collected and frozen at -80 °C, and the remaining blood cell pellet was resuspended
743 in erythrocyte lysis buffer (83 g/L NH_4Cl, 8.5 g/L $NaHCO_3$, 10 mM EDTA) and
744 incubated at 37 °C for 6 min for peripheral blood cell (PBC) isolation. After
745 centrifugation at 400 g for 5 min (RT), supernatant was discarded and cells underwent

746 a second erythrocyte lysis step (37 °C, 4-6 min). Reaction was stopped using ice-cold
747 PBS + 0.5 % BSA + 2 mM EDTA (referred to as FACS buffer) and cell suspension was
748 filtered through a 30 µm strainer.

749 Spleens were excised and kept in FACS buffer at 4 °C. Single cell suspensions were
750 obtained by pressing tissue through 70 µm EasyStrainer, followed by erythrocyte lysis
751 and filtration through 40 µm EasyStrainer.

752 Hearts were excised, atria were removed and tissue was kept in HBSS without
753 Ca^{2+}/Mg^{2+} + 10 mM HEPES (referred to HBSS w/o) at 4 °C. Ventricles were cut into 2-
754 3 mm pieces before transfer into gentleMACS C Tubes (Miltenyi Biotec). A fresh
755 digestion mix was prepared with DNase I (30 U/mL), Hyaluronidase I-S (60 U/mL),
756 Collagenase XI (125 U/mL) in 1 mL HBSS with Ca^{2+}/Mg^{2+}. Samples were incubated
757 for 1 h at 700 rpm and 37 °C, followed by mechanical dissociation using the
758 gentleMACS Octo Dissociator (Miltenyi Biotec, program m_heart_02). Digestion was
759 quenched using ice-cold PBS + 10 % FBS. Cells were pelleted (400 g, 10 min, 4 °C),
760 treated with erythrocyte lysis buffer for 3 min at RT, neutralized with FACS buffer, and
761 filtered sequentially through 70 µm and 40 µm EasyStrainers. An aliquot was collected
762 for absolute counting (1:100 dilution).

763 Intestines were excised, flushed with HBSS w/o to remove all contents, divided into
764 small intestine (duodenum, jejunum, ileum) and large intestine (cecum, colon) and
765 stored in HBSS w/o at 4 °C. Lamina propria cells were isolated using the Lamina
766 Propria Dissociation Kit, mouse (Miltenyi Biotec).

767 Heart and lamina propria cell suspensions were subjected to a 40%/80% Percoll
768 density gradient (centrifugation at 800 g, 20 min, RT, no brake). Immune cells were
769 harvested at the interphase and washed in FACS buffer.

770 Splenocyte and lamina propria cell suspensions were counted on a LUNA-FL Dual
771 Fluorescence Cell Counter (Logos Biosystems), centrifuged and resuspended at
772 $1x10^6$ cells per 100 µL medium (RPMI 1640 + 10% FBS + 1% penicillin/streptomycin
773 [P/S, 10,000 U/mL / 10,000 µg/mL]) for further analysis. PBC and heart cell
774 suspensions were directly centrifuged and resuspended in 100 µL medium per flow
775 cytometry panel.

776 Cells were either immediately stained for flow cytometry or restimulated with 50 ng/mL
777 PMA, 500 ng/mL ionomycin, and 0.75 µL/mL GolgiStop in medium for 4 h at 37 °C, 5 %

778 CO_2. Viability was assessed with Live/Dead Fixable Aqua for 405 nm (Thermo Fisher),
779 surface markers were stained in Brilliant Stain Buffer (BD Biosciences) with Fc block
780 (Miltenyi Biotec), then cells were fixed/permeabilized (eBioscience
781 FoxP3/Transcription Factor Buffer Kit) for intracellular staining. All antibody
782 incubations were 30 min at 4 °C (Table S7). Data were acquired on a BD LSRFortessa
783 with high throughput sampler (HTS) using BD FACSDiva and analyzed in
784 FlowJo 10.8.1.

785

786 Flow cytometry analysis

787 Immune cell populations were identified by flow cytometry using the gating strategies
788 in Figure S9. For the immune cell abundance analysis, batch effects arising from
789 different flow cytometry acquisition days were corrected using ComBat from the *sva* R
790 package (v.3.20). Raw abundance values were imported into R and the matrix of cell-
791 type frequencies was extracted. Batch identifiers were supplied as the batch variable,
792 and group assignment was included as a covariate in the ComBat model matrix.
793 ComBat was run with parametric priors and without generating prior plots, yielding
794 batch-adjusted abundance values that were re-combined with sample metadata for
795 downstream analyzes. All subsequent analyzes were performed on the batch-
796 corrected dataset using the same gating-based cell populations described above.
797 UMAP visualizations were generated from the T-cell panel using two representative
798 samples per group. $CD3^+$ T cells were isolated using the hierarchical gating strategy,
799 and all gated events (10,000 $CD3^+$ T cells per sample) were used for dimensionality
800 reduction. UMAP embeddings were computed in FlowJo using the UMAP_R plugin
801 (version 4.1.1) with Euclidean distance, minimum distance = 0.1, and 15 nearest
802 neighbours. FlowJo's default logical transformation was applied to all fluorescence
803 channels. Group-level embedding intensity plots were created in FlowJo by overlaying
804 all cells from the same group and visualizing them as smoothed density distributions.

805

806 **Mouse AhR reporter assay**

807 Mouse AhR-responsive reporter cell line (H1L1.1c2), derived from mouse hepatoma
808 (Hepa1c1c7) cells and stably transfected with the pGudLuc1.1 vector containing AhR-
809 responsive dioxin response elements (DRE) upstream of a luciferase gene, was kindly

810 provided by Prof. Michael S. Denison, University of California, Davis, CA, USA.
811 H1L1.1c2 cells were cultured in Opti-MEM (Thermo Fisher, 31985070) supplemented
812 with 1% FBS (Merck, F7524), 1% P/S, and 0.2 mg/mL G418 (Sigma, A1720-1G), and
813 maintained at 37 °C with 5% CO_2. Subculture was performed twice a week using
814 TrypLE™ Express Enzyme (Gibco, 12604-02).

815 For the assay, cells were seeded in 96-well plates at a density of $7.5x10^4$ cells/well
816 and allowed to attach for 24 h. Cells were then incubated with 10% mouse plasma in
817 the same medium for 24 h. Assays were performed in triplicate, and 6-formylindolo[2-
818 b]carbazole (FICZ) was included as a positive control at a concentration of 10 nM.
819 After treatment, luciferase activity and cell viability were quantified using the One-
820 Glo™ + Tox Luciferase Reporter and Cell Viability Assay (Promega, E7120) according
821 to the manufacturer's instructions. Luminescence and fluorescence were measured
822 using a microplate reader (Infinite 200 plate reader, Tecan). Luminescence values
823 were normalized to cell viability (fluorescence signal) and subsequently expressed
824 relative to the FICZ control within each plate.

825

826 **T_H17 polarization assay, murine**

827 Mesenteric and peripheral lymph nodes (LN) were harvested from 129S2/SvPasOrlRj
828 mice and kept in cold FACS Flow buffer. LN were mechanically dissociated through a
829 70 µm cell strainer using cold FACS Flow buffer. The cell suspension was
830 subsequently filtered through a 40 µm strainer, washed with 20 mL FACS Flow buffer,
831 and centrifuged at 400 × g for 10 minutes at 4°C. Cells were resuspended in FACS
832 Flow buffer at 1 × 10^7 cells per 100 µL.

833 CD4+ T cells were enriched via magnetic-activated cell sorting (MACS) using the
834 MojoSort Mouse CD4 T Cell Isolation Kit (BioLegend) with minor modifications for the
835 use of magnetic columns. Briefly, cells were incubated with a biotinylated antibody
836 cocktail (2 µL per 10^7 cells in 100 µL) for 15 minutes at 4°C, followed by Streptavidin
837 Nanobeads (2 µL per 10^7 cells) for an additional 15 minutes at 4°C. Cells were
838 separated using LS columns (Miltenyi Biotec) and the unlabelled fraction was used for
839 further analysis. For naïve CD4+ T cell isolation, cells were stained with CD4
840 (VioGreen), CD25 (PE), CD44 (BB700), CD62L (BV421), and a live/dead stain

841 (Zombie Green) and $CD4^{+}CD25^{-}CD44^{low}CD62L^{high}$ cells were sorted on a FACS
842 Melody (BD Bioscience, 100 µm nozzle).

843 96-well flat-bottom plates were coated overnight at 4°C with anti-CD3 antibody (2
844 µg/mL in PBS, 50 µL per well). Naïve CD4+ T cells were resuspended in T_H17
845 differentiation medium (RPMI-1640 supplemented with 10% FCS, 1% penicillin-
846 streptomycin, 1% L-glutamine, 1% non-essential amino acids, 1 mM sodium pyruvate,
847 and 0.01 mM β-mercaptoethanol). Cells were plated at 5 × 10^4 cells per well in a final
848 volume of 200 µL with anti-CD28 (2 µg/mL), mIL-6 (80 000 U/mL, Miltenyi Biotec),
849 rhTGFβ1 (40 U/mL, Miltenyi Biotec) and mIL-1β (33 600 U/mL, Miltenyi Biotec) and
850 test compounds (IxS, KCl, AhRi at concentrations indicated in the respective figure) or
851 DMSO vehicle control, as appropriate. Cells were cultured at 37°C with 5% CO_2 for 4
852 to 5 days and subsequently restimulated for 4 hours with PMA (50 ng/ mL), ionomycin
853 (750 ng/mL), and GolgiPlug (0.5 µL/mL). Following restimulation, cells were washed
854 with FACS Flow buffer, stained with BD Horizon Fixable Viability Stain 700 (1:500
855 dilution) for 30 minutes cold, fixed, and permeabilized using Fix/Perm buffer
856 (eBioscience), and stained with the antibodies indicated in Table S7. Cells were
857 analyzed using a BD LSRFortessa with high throughput sampler (HTS). Data were
858 processed using FlowJo.

859

860 **RNA isolation**

861 Splenocytes were isolated as described above, enriched for CD45+ using mouse
862 CD45 MicroBeads (Miltenyi Biotec). Hearts were excised and apex was snap frozen
863 at -80°C. Spleens were excised and a small piece of tissue was placed into 300 µL
864 RNAprotect Tissue Reagent (Qiagen) at 4 °C for a minimum of 24 h. RNAprotect
865 Tissue Reagent was then discarded, and tissues were frozen at -80 °C.

866 RNA isolation from splenocytes and spleen was performed using the RNeasy Mini Kit
867 (Qiagen). RNA isolation from heart was performed using the RNeasy Fibrous Tissue
868 Mini Kit (Qiagen). For cell homogenisation, enriched CD45+ splenocytes were
869 resuspended in buffer RLT + β-mercaptoethanol and vortexed vigorously. Tissue
870 pieces were immersed in RLT buffer + β-mercaptoethanol with 1.5 mm ceramic beads
871 and placed into a Precellys 24 tissue homogeniser. RNA was subsequently isolated
872 from both sample types according to the instructions of the respective kits.

873 Fibroblasts on well plates were washed in PBS and incubated with 700 µL Qiazol Lysis
874 Reagent (Qiagen) per well at -80 °C over night. Then, lysed cells were harvested,
875 transferred to a tube and vortexed vigorously. 200 µL of chloroform was added and
876 samples were centrifuged at 12,000 g for 15 min at 4 °C. Afterwards, the aqueous
877 phase was collected and RNA was isolated with the RNeasy Mini Kit according to the
878 manufacturer's protocol.

879

880 **Quantitative polymerase chain reaction (qPCR)**

881 All qPCR was performed on a QuantStudio™ 5 Real-Time PCR System (Thermo
882 Fisher Scientific) using a 384-well plate format. For each 5-µL reaction mix, 4 ng of
883 DNA or cDNA was used, and all detections were performed in triplicate. All primer and
884 probe sequences and concentrations are listed in Table S6.

885 For all SYBR-Green based detection, the PowerUP™ SYBR™ Green Master Mix
886 (Thermo Fisher Scientific) was used with a fast cycling protocol of 50 °C for 2 min, 95
887 °C for 2 min, followed by 40 cycles of 95 °C for 1 s and 60 °C for 30 s. For all TaqMan-
888 based detection, the TaqMan® Multiplex Master Mix (Thermo Fisher Scientific,
889 4461882) was used with a fast cycling protocol of 95 °C for 20 s, followed by 40 cycles
890 of 95 °C for 2 s and 60 °C for 20 s.

891 For *16S* quantification, cecal DNA was amplified and detected using SYBR Green and
892 the standard curve method. Standard curves were generated using 10-fold serial
893 dilutions ranging from 10^1 to 10^9 copies of the *16S* rRNA gene of *E. coli* (Invitrogen)
894 amplified with primers 27F (5′-GTTTGATCCTGGCTCAG-3′) and
895 1492R (5′-CGGCTACCTTGTTACGAC-3′). Using the resulting curve, *16S* rDNA copy
896 numbers per gram content were calculated.

897 For all other genes, cDNA was synthesized prior to qPCR using the High Capacity
898 cDNA Reverse Transcription Kit (Thermo Fisher Scientific). Murine *Col1a2*, *Acta2*,
899 *Cyp1a1* and *18s* were detected using TaqMan. Gene expression was normalized to
900 the *18s* signal using the ΔΔCt method. All other murine genes were quantified using
901 SYBR Green, and *Hprt* or *Gapdh* as the housekeeping genes. All human genes were
902 quantified using SYBR Green and normalized to *HPRT1* using the ΔΔCt method. All
903 primer and probes are shown in Table S6.

904 **Bulk mRNA sequencing**

905 Illumina stranded mRNA library preparation and bulk mRNA sequencing were
906 performed at the BIH/MDC Genomics Technology Platform. Paired-end sequencing
907 was performed on an Illumina NovaSeq X Plus platform, targeting ~30 million reads
908 per sample. Transcript quantification of raw sequencing data to the *Mus musculus*
909 reference transcriptome (GRCm38) was performed using Salmon (v1.10.1). Quality
910 assessment of the preprocessing was performed using MultiQC (v1.6). Following
911 quality control, 26.4M-34.7M paired-end reads per sample were retained and included
912 in downstream analysis. Gene symbols were generated from Ensembl gene IDs using
913 biomaRt (v2.52.0, Ensembl release 102). Post-processing quality control and
914 downstream data analysis were conducted using DESeq2 (v1.42.1).

915 For the Abx trial, separate DeSeq2 datasets were generated for each reference
916 condition (Sham, STNx). Lowly expressed genes were removed by filtering for
917 transcripts with at least 1 count per million in a minimum of two samples using edgeR
918 (v4.0.16). Differential expression analysis was performed using the DeSeq2 pipeline.
919 Log_2 fold changes were adjusted using lfcShrink with the ashr method (v2.2.63), and
920 p-values were corrected using a false discovery threshold of 10%. Variance-stabilized
921 expression values were obtained using the rlog transformation.

922 Gene set enrichment analysis (GSEA) was performed on the overlap of significantly
923 regulated genes from the STNx vs. Sham and STNx Abx vs. STNx comparisons
924 (adjusted p-value < 0.1). Curated *Mus musculus* gene sets were downloaded from
925 MSigDB. Enrichment was calculated with Fisher's exact test and FDR correction,
926 using all Ensembl gene IDs present in the complete MSigDB *Mus musculus* dataset
927 as the background. Pathways and GO terms not relevant to the study were excluded
928 from visualisation using targeted keyword filtering.

929 For the AhRi trial, differential expression analysis with DeSeq2 was restricted to the
930 set of DEGs in STNx that were Abx responsive. Batch effects between experimental
931 rounds were corrected using ComBat-seq (sva, v3.50.0). Genes significantly regulated
932 by AhRi-treatment in the same direction as the Abx-dependent response ($p < 0.1$)
933 were subjected to GSEA.

934 For both trials, targeted gene set variation analysis (GSVA) was performed on rlog-
935 transformed expression values using curated gene sets relevant to the T_H17 axis (gsva
936 package, v1.50.5).

937

938 **Single-cell RNA-sequencing**

939 We analyzed publicly available mouse cardiac single-nucleus and human single-cell
940 RNA-seq datasets[32,37]. Processed Seurat objects were imported into R (v4.2.2) using
941 Seurat (v5.0). No reclustering or reannotation was performed. For each dataset, cells
942 belonging to diseased samples (mouse CKD or human CKD) and appropriate controls
943 were subset for downstream analyzes. Resident structural cell types were selected
944 based on the original annotations, and expression of IL17ra was quantified from log-
945 normalized RNA values to identify positive and negative stromal populations.
946 Extracellular matrix (ECM) activity was assessed using an extended NABA matrisome
947 gene list[33] and compared using Wilcoxon tests. AhR pathway activity was similarly
948 scored using a recently published AhR-responsive gene set[60]. Differential expression
949 was performed using the MAST framework[61], including only genes expressed in more
950 than 10% of nuclei. Genes were considered differentially expressed when meeting:
951 adjusted $p < 0.1$, absolute $\log_2$ fold change > 0.3, and average normalized expression
952 > 3 in Il17ra$^+$ cells. Differentially expressed genes were compared with curated
953 fibroblast transcriptional signatures derived from human cardiac and stromal
954 datasets[34] to identify enriched transcriptional programs. Briefly, DEG were intersected
955 with each fibroblast signature and the number of overlapping genes, proportion of
956 signature genes present among upregulated genes, and average FC and expression
957 of the overlapping genes were used to find similar transcriptional programs. Cytokine-
958 response enrichment was conducted from DEG of cardiac lymphocytes as described
959 above using the Immune Response Enrichment Analysis (IREA)[62] software.

960

961 **Murine cardiac fibroblasts**

962 Hearts were freshly harvested from 7-10 weeks old male and female C57BL/6J mice
963 and rinsed twice in PBS. Aortic and atrial tissues were removed, and ventricles were
964 minced and transferred into 1 mL of enzymatic digestion solution containing DNase I
965 (300 U/mL), Hyaluronidase I-S (60 U/mL), Collagenase XI (125 U/mL), and

966 Collagenase I (450 U/mL) in DMEM. Digestion was performed on a shaking incubator
967 (800 rpm, 37 °C) for 45 minutes.

968 Following digestion, the cell suspension was filtered through a 70 µm strainer using
969 PBS and centrifuged at 400 g for 10 minutes at 37 °C. The pellet was resuspended in
970 1 mL erythrocyte lysis buffer (Erylysis), incubated for 3 minutes at RT, and quenched
971 with PBS. Cells were centrifuged again under the same conditions, supernatant was
972 discarded, and the pellet was resuspended in 4 mL fibroblast culture medium (DMEM
973 supplemented with 20% FBS, 2% penicillin-streptomycin, 1 ng/mL endothelial cell
974 growth factor [ECGF], and 10 µg/mL heparin). Cells were maintained at 37 °C and 5%
975 CO_2. Media was changed after 2.5 h and further replaced every 2-3 days. For
976 subculture, fibroblasts were detached using Trypsin-EDTA (1mL, 2-3 min incubation).
977 Reaction was stopped with culture media, fibroblasts were transferred to a 15 mL tube
978 and centrifuged at 400 g for 10 min. Pellet was resuspended in culture media, counted
979 and plated into tissue flasks or well plates depending on cell counts (6.000-10.000
980 cells/cm^2).

981 Assay was performed on a 6-well plate. In brief, fibroblasts were starved in culture
982 media containing 1% FBS and incubated for 4 h at 37 °C, followed by a 24 h incubation
983 with the test substances. Murine recombinant IL-17A was used at 1 ng/mL in culture
984 media. Potassium 3-indoxyl sulfate was used at 50 µM and 100 µM on its own, and at
985 100 µM in combination with IL-17A in culture media. After 24 hours incubation,
986 fibroblasts were washed in PBS and incubated with 700 µL Qiazol Lysis Reagent per
987 well at -80 °C over night. Lysed fibroblasts were then harvested, RNA was isolated
988 and RT-qPCR was performed as described above.

989 For immunofluorescence staining, 18x18 mm coverslips were sterilized with ethanol
990 70% and placed into 6-well plates. Fibroblasts were grown on the coverslips in culture
991 media until desired confluence. Cells were then washed with PBS and fixed with 4%
992 Paraformaldehyde, followed by permeabilization with 0.1% Triton X-100 and blocking
993 with 10% normal donkey serum (NDS) in PBS.

994 For PDGFRα and VIM staining, cells were incubated with conjugated antibodies (anti-
995 mouse CD140a PE, 1:100, clone APA5, Miltenyi, 130-102-502 and AF647 anti-
996 vimentin, 1:500, clone EPR3776, ab194719) for 2 h at RT in PBS + 10% NDS. For
997 COL-1 and IL17RA staining, cells were incubated with primary antibodies (goat anti-

998 type I collagen, 1:500, polyclonal, Southern Biotech, 1310-01 and rabbit anti-IL17RA,
999 1:500, polyclonal, abcam, ab180904) for 2 h at RT in PBS + 10% NDS. After washing
1000 with PBS + 1% NDS, secondary antibodies, donkey anti-rabbit IgG Alexa Fluor Plus
1001 488 (1:1000, Thermo Fisher) and anti-goat IgG Alexa Plus 555 (1:1000, Thermo
1002 Fisher), were incubated together with DAPI (1:1000, Biotium) in PBS + 10% NDS for
1003 1 h at RT. After washing, coverslips were taken out of the well plates and mounted
1004 onto microscopy slides using DAKO fluorescent mounting medium. Slides were
1005 imaged on the Keyence Compact Fluorescence microscope with the Plan Apochromat
1006 20x objective lens.

1007 For flow cytometry staining, cells were stained for PDGFRα, CD45 and CD31
1008 (antibody concentrations in Table S7) together with SYTOX™ Green Dead Cell Stain
1009 (1:500, Invitrogen, S34860) and Fc blocking reagent (Miltenyi Biotec, 130-092-575) in
1010 FACS buffer. Data were acquired on a BD LSRFortessa using BD FACSDiva and
1011 analyzed in FlowJo 10.8.1.

1012

1013 **Splenocyte incubation assay**

1014 Spleens from 129S2/SvPasOrlRj mice were processed to obtain spleen single-cell
1015 suspensions as described above. For *ex vivo* stimulation, splenocytes were incubated
1016 for 4 h at 37 °C, 5 % CO_2 in RPMI-1640 in the presence of IxS and AhRi at the indicated
1017 concentrations. After incubation, cells were resuspended in buffer RLT + β-
1018 mercaptoethanol and frozen at −80 °C for subsequent RNA isolation as described
1019 above.

1020

1021 **Patient serum collection**

1022 Patients with CKD stage 5 dependent on hemodialysis were recruited Department of
1023 Nephrology and Medical Intensive Care at Charité-Universitätsmedizin Berlin. Healthy
1024 volunteers were recruited at the Experimental and Clinical Research Center (ECRC)
1025 of Charité-Universitätsmedizin Berlin. Ethical approval was obtained from the
1026 institutional review board of Charité–Universitätsmedizin Berlin (EA2/162/17) and all
1027 participants provided written informed consent before biomaterial was collected. Blood
1028 was obtained from patients at the start of hemodialysis. Serum was collected by

1029 centrifugation at 1500 g for 15 min at RT, and stored at -80 °C until further use.
1030 Demographic and clinical characteristics of the study cohort are summarized in Table
1031 S4.

1032

1033 **Human luciferase reporter assay**

1034 Human AhR reporter cell line (HT29-Lucia™ AhR, InvivoGen, ht21-ahr), containing
1035 AhR-responsive DRE upstream of a Lucia luciferase gene, was cultured in Dulbecco's
1036 Modified Eagle Medium (DMEM) supplemented with 10% FBS and 100 µg/mL Zeocin
1037 (InvivoGen, ant-zn-05), maintained at 37 °C with 5% CO_2. Cells were subcultured once
1038 per week using a standard Trypsin-EDTA protocol and partially replenished with fresh
1039 medium mid-week between passages.

1040 For the assay, 180 µL of cell suspension per well was seeded on a 96-well plate at a
1041 density of 2.8×10^5 cells/mL in medium without Zeocin. For the dose-response curve of
1042 AhRi, cells were incubated with 100 µM IxS and AhRi concentrations between 1 nM
1043 and 10 µM or VEH (vehicle, DMSO content of the highest AhRi concentration) for 24
1044 h in quadruples. To assess the AhR activation potential of human biomaterial, cells
1045 were incubated with 10% patient serum and AhRi in a final concentration of 1 or 0.1
1046 µM, or VEH for 24 h in triplicates. For quantification, 20 µL of culture supernatant was
1047 used to determine luciferase activity using the QUANTI-Luc™ Luciferase Detection
1048 Reagent (InvivoGen, rep-qlc4lg1). Luminescence was measured using a microplate
1049 reader (Infinite 200 plate reader, Tecan).

1050

1051 **Human T_H17 polarization assay**

1052 Peripheral blood mononuclear cells (PBMC) were collected together with serum from
1053 healthy volunteers under the ethics approval described above (EA2/162/17). PBMC
1054 were isolated from EDTA-anticoagulated blood of a healthy donor by diluting samples
1055 1:1 in PBS + 2% FBS and layering them into 50 mL SepMate tubes (Stemcell) prefilled
1056 with 15 mL Pancoll (PAN Biotech). After centrifugation at 1200 g for 10 min at RT, the
1057 mononuclear cell layer was collected, transferred into a fresh 50 mL tube, and washed
1058 with PBS + 2% FBS, followed by erythrocyte lysis.

1059 T cells were isolated from PBMC using MojoSort Human CD4 T Cell Isolation Kit
1060 (Biolegend) with LS columns (Miltenyi) following the manufacturer's protocol. To obtain
1061 naïve CD4 cells, the enriched T helper cell fraction was sorted using a BD FACSAria
1062 III (BD Bioscience, 70 µm nozzle) by staining for CD4, CD25, CD127, CD45RO (Table
1063 S8), and dead cells exclusion with DRAQ7 (1:250, Miltenyi Biotec).

1064 Naïve CD4 T cells were resuspended in X-VIVO 15 serum-free hematopoietic media
1065 (Lonza Bioscience) and plated at $5x10^4$ cells per well in anti-CD3-coated (10 µg/mL,
1066 BD) 96-well U-bottom plates and 1 µg/mL anti-CD28 (BD). To induce T_H17
1067 polarization, naïve CD4 T cells were cultured with 12.5 ng/mL IL-1β, 25 ng/mL IL-6,
1068 25 ng/mL IL-21, 25 ng/mL IL-23, and 5 ng/mL TGF-β (all Miltenyi Biotec), while T_H0
1069 control wells were left without cytokine supplementation. Cells were treated with 2.5%
1070 serum from either hemodialysis patients or healthy controls in triplicates and
1071 maintained for 7 days at 37°C and 5% CO2.

1072 Prior to analysis, cells were restimulated for 4 h with 10 ng/mL PMA (Merck), 500
1073 ng/mL ionomycin (Merck), and 1 µL/mL GolgiPlug (BD), stained with LIVE/DEAD
1074 fixable aqua dye (Invitrogen), fixed and permeabilized using the Foxp3/Transcription
1075 Factor Staining Buffer Set (Invitrogen), and finally stained with antibody panels with
1076 Fc Block, CD4 and IL-17A (antibodies listed in Table S8).

1077 Cells were analyzed using a BD LSRFortessa with HTS and data were processed
1078 using FlowJo (v10.10).

1079

1080 **UK Biobank**

1081 Study participants

1082 The UK Biobank is a population-based cohort of 502,366 participants aged 40-69
1083 years recruited between 2006 and 2010 across 22 assessment centers in England,
1084 Scotland, and Wales. Ethical approval was granted by the North West Multi-Centre
1085 Research Ethics Committee (reference 11/NW/0382), and all participants provided
1086 written informed consent. Data available as of 16 November 2023 were used for this
1087 study.

1088 Participants with impaired kidney function were defined as those with an estimated
1089 glomerular filtration rate (eGFR) below 60 mL/min/1.73 m², corresponding to KDIGO

categories G3-G5. Demographic and clinical characteristics of the study cohort are summarized in Table S5.

Identification of individuals with heart failure with preserved ejection fraction (HFpEF) followed a previously published multi-stage algorithm[63]. All HFpEF cases were required to exhibit at least one clinical symptom of heart failure in accordance with European Society of Cardiology (ESC) guidelines, supplemented by additional criteria depending on data availability. When cardiac magnetic resonance (CMR) imaging was available, participants with a left ventricular ejection fraction above 49% were considered to have preserved systolic function. When NT-proBNP measurements were available, patients exceeding the 90th percentile were classified as HFpEF, whereas those with lower values or evidence of reduced ejection fraction were excluded. For participants lacking imaging or proteomic data, HFpEF was assigned when the pre-test probability exceeded 90%.

Data modalities

All variables used in this study were assessed prior to or at the baseline visit. eGFR was calculated from plasma cystatin C concentrations using the equation eGFR = 74.835 / (cystatin $C^{1.333}$). Albuminuria was quantified as the urine albumin-to-creatinine ratio. Essential hypertension was defined by the presence of an ICD-10 I10 diagnosis code recorded before baseline. Proteomics profiling was available for approximately 10% of the UK Biobank participants and was performed using Olink proximity extension assays, with protein concentrations reported as $\log_2$-normalized protein expression (NPX) values. For the present analysis, we focused on NT-proBNP and IL-17A, which were available for 51,578 and 50,573 participants, respectively. Smoking exposure was quantified using the UK Biobank variable “pack years of smoking” (Field-ID 20161), calculated from baseline questionnaire responses using the formula: (cigarettes per day / 20) * (age stopped smoking - age started smoking). This measure reflects cumulative smoking intensity, with higher values reflecting greater lifetime exposure.

Statistical Analysis

Time-to-event outcomes were evaluated using Kaplan-Meier estimators implemented in the Python package lifelines (version 0.30.0). Participants were stratified into three IL-17A groups according to the plasma IL-17A concentrations: below the 25th

1122 percentile, between the 25th and 75th percentiles, and above the 75th percentile.
1123 Survival time was defined as the interval from baseline to the occurrence of the event
1124 of interest, with censoring at the end of follow-up. Differences across IL-17A strata
1125 were assessed using the log-rank test.

1126 To evaluate the association between IL-17A and clinical outcomes, Cox proportional
1127 hazards models were fitted. All covariates were standardized before model fitting to
1128 facilitate direct comparison of effect sizes. Cox proportional hazards models were
1129 estimated using an unpenalized framework with robust variance estimation. To ensure
1130 numerical stability, a limited grid of ridge penalisation terms ($\lambda = 0$ to 0.01) was
1131 evaluated, and the model yielding stable convergence without materially influencing
1132 effect estimates was selected. Hazard ratios (HRs) and 95% confidence intervals (CIs)
1133 were derived from the final model and displayed using forest plots.

1134 Normality of continuous variables was assessed using the Shapiro-Wilk test. When
1135 both groups satisfied the normality assumption ($p > 0.05$), differences were evaluated
1136 using Welch's *t* test; otherwise, comparisons were performed using the non-parametric
1137 Mann-Whitney U test. For analyzes involving multiple statistical tests, p-values were
1138 adjusted using the Benjamini-Hochberg false discovery rate (FDR) procedure. All
1139 statistical analyzes were performed in Python 3.11.

1140

1141 **Human cardiac fibroblasts**

1142 Human cardiac fibroblasts were obtained from PromoCell (Germany). Cells were
1143 seeded (4000 cells per cm^2 seeding density) with 18 mL of Fibroblast Growth
1144 Medium 3 (PromoCell, Germany) into a tissue flask T75. Media contained
1145 supplements (PromoCell, Germany), P/S (1%) and Amphotericin B (Gibco, 0.2%).
1146 Cells were maintained at 37 °C and 5% CO_2 with medium exchanged every 2-3 days
1147 and passaged at 70-90% confluence as described above. Subculture was performed
1148 using the standard Trypsin-EDTA protocol.

1149 For all experiments, cells were seeded at manufacturer recommended densities and
1150 allowed to attach overnight. The following day, cultures were starved for 4h in medium
1151 containing 1% FBS and subsequently stimulated for 24h under the appropriate
1152 conditions. Treatments included IL-17A (1 ng/mL), IxS (100 µM), AhRi (1 µM),
1153 Secukinumab (Cosentyx, 10 nM), human serum (HD/HC; 10%), or the corresponding

combinations. After stimulation, cells were washed once with PBS and lysed in QIAzol as descrived above. Lysed cells were then harvested, RNA was isolated and RT-qPCR was performed as described above.

To assess viability and proliferation, fibroblasts were co-incubated of IL-17A and IxS in starved medium for 24 h. After detaching, cells were stained with Zombie Green Fixable Viability Kit (1:500, BioLegend), fixed/permeabilized (eBioscience FoxP3/Transcription Factor Buffer Kit) for intracellular staining, and stained for Ki-67 (Table S8.)

Data and code availability

All code, data, and scripts used in this study will be made publicly available. The code and scripts will be made accessible on Zenodo. The raw sequencing data will be deposited in the NCBI Sequence Read Archive.

Author contribution

CRediT: Conceptualization: AY, WA, AT, JH, HB, NW; Data curation: AY, WA, JVe, HA, MK; Formal Analysis: AY, WA, OP; Funding acquisition: VM, UK, AZ, PO, WG, KUE, DNM, MK, HB, NW; Investigation: AY, WA, AT, OP, FS, IAS, AMR, JVe, NG, VM, SH, SK, GT, HA, FF, CH, SAH, PMB, MIW, FB; Methodology: AY, WA, OP, FS, IAS, JVe, JVo, PO, WG, KD, MK, HB, NW; Project administration: AY, WA; Resources: UK, TK, BK, AZ, PO, WG, KD, KUE, DNM, MK, JH, HB, NW; Software: AY, WA, JVe, HA; Supervision: JVo, UK, TK, BK, AZ, PO, WG, KD, KUE, DNM, MK, JH, HB, NW; Validation: AY, WA, RK, MK; Visualization: AY, WA, JVe, HB, NW; Writing - original draft: AY, WA, HB, NW; Writing - review & editing: all authors.

Acknowledgment

We thank Melanie Röhr and Gudrun Koch for their technical assistance, Ilona Kamer for the implantation of the blood pressure telemetry devices and Heike Schwede for support with animal husbandry. We also thank Laura Mossier for contributing to the HFpEF trial, and Daniel Herrmann for his technical assistance with the IxS quantification. Clinical chemistry and echocardiography measurements were performed at the Preclinical Research Center of the MDC. Bulk mRNA-seq was performed at the BIH/MDC Genomics Technology Platform. Human T cells were sorted using the flow cytometry platform of the MDC. We thank the MDC Max Cluster for providing us with the scientific compute cluster resources and Ulrike Löber for bioinformatics support.

Funding

FACSMelody used in this study was funded by German Federal Ministry of Research, Technology and Space (BMFTR), project-ID: 01EJ2202A. V.M., D.N.M., W.G., P.J.O., H.B., and N.W. were supported by the BMFTR, TAhRget consortium (project-ID 01EJ2502A (N.W.), 01EJ2502B (W.G., P.J.O.), 01EJ2502E (V.M., D.N.M.), and 01EJ2502G (H.B.)), as well the QEED consortium (project-ID 13N16386, to H.B.). U.K., D.N.M., A.Z. and N.W. were supported by the German Research Foundation (DFG), CRC1470 (project-ID 437531118, subproject A10 to N.W., A06 to D.N.M., and A09 to U.K.), and CRC1525 (project-ID 453989101, to A.Z.) and project-ID 432915089

(to A.Z). D.N.M. and N.W. were supported by the DZGIF (DZG Innovation Fund), Topic "Microbiome". N.W. was supported from the European Research Council (ERC) under the European Union's Horizon 2020 research and innovation program (852796). N.W. was supported by the Corona Foundation in the German Stifterverband (S199/10080/2019). K.U.E. received funding from the European Union's Horizon 2020 research and innovation program under a Marie Skłodowska-Curie Innovative Training Networks (H2020-MSCA-ITN-2019) grant (TrainCKDis, project-ID 860977).

Conflict of interest

The authors declare no conflict of interest.

References

1 Langenberg, C., Hingorani, A. D. & Whitty, C. J. M. Biological and functional multimorbidity—from mechanisms to management. *Nature Medicine* **29**, 1649-1657 (2023). https://doi.org/10.1038/s41591-023-02420-6

2 Evenepoel, P., Poesen, R. & Meijers, B. The gut-kidney axis. *Pediatr Nephrol* **32**, 2005-2014 (2017). https://doi.org/10.1007/s00467-016-3527-x

3 Eckardt, K.-U. *et al.* Evolving importance of kidney disease: from subspecialty to global health burden. *The Lancet* **382**, 158-169 (2013). https://doi.org/10.1016/S0140-6736(13)60439-0

4 Mishima, E. *et al.* Evaluation of the impact of gut microbiota on uremic solute accumulation by a CE-TOFMS–based metabolomics approach. *Kidney International* **92**, 634-645 (2017). https://doi.org/https://doi.org/10.1016/j.kint.2017.02.011

5 Mair, R. D., Sirich, T. L., Plummer, N. S. & Meyer, T. W. Characteristics of Colon-Derived Uremic Solutes. *Clin J Am Soc Nephrol* **13**, 1398-1404 (2018). https://doi.org/10.2215/cjn.03150318

6 Jankowski, J., Floege, J., Fliser, D., Böhm, M. & Marx, N. Cardiovascular Disease in Chronic Kidney Disease. *Circulation* **143**, 1157-1172 (2021). https://doi.org/doi:10.1161/CIRCULATIONAHA.120.050686

7 Speer, T., Dimmeler, S., Schunk, S. J., Fliser, D. & Ridker, P. M. Targeting innate immunity-driven inflammation in CKD and cardiovascular disease. *Nature Reviews Nephrology* **18**, 762-778 (2022). https://doi.org/10.1038/s41581-022-00621-9

8 Wilck, N. *et al.* Salt-responsive gut commensal modulates T(H)17 axis and disease. *Nature* **551**, 585-589 (2017). https://doi.org/10.1038/nature24628

9 Granados, J. C. *et al.* AHR is a master regulator of diverse pathways in endogenous metabolism. *Scientific Reports* **12**, 16625 (2022). https://doi.org/10.1038/s41598-022-20572-2

10 Rothhammer, V. & Quintana, F. J. The aryl hydrocarbon receptor: an environmental sensor integrating immune responses in health and disease. *Nature Reviews Immunology* **19**, 184-197 (2019). https://doi.org/10.1038/s41577-019-0125-8

11 Dong, F. & Perdew, G. H. The aryl hydrocarbon receptor as a mediator of host-microbiota interplay. *Gut Microbes* **12**, 1859812 (2020). https://doi.org/10.1080/19490976.2020.1859812

12 Gutiérrez-Vázquez, C. & Quintana, F. J. Regulation of the Immune Response by the Aryl Hydrocarbon Receptor. *Immunity* **48**, 19-33 (2018). https://doi.org/10.1016/j.immuni.2017.12.012

13 Anandakumar, H. *et al.* Segmental patterning of microbiota and immune cells in the murine intestinal tract. *Gut microbes* **16**, 2398126 (2024). https://doi.org/10.1080/19490976.2024.2398126

14 Voroneanu, L. *et al.* Gut Microbiota in Chronic Kidney Disease: From Composition to Modulation towards Better Outcomes-A Systematic Review. *J Clin Med* **12** (2023). https://doi.org/10.3390/jcm12051948

15 Chaves, L. D. *et al.* Chronic kidney disease, uremic milieu, and its effects on gut bacterial microbiota dysbiosis. *Am J Physiol Renal Physiol* **315**, F487-f502 (2018). https://doi.org/10.1152/ajprenal.00092.2018

16 Bloom, P. P. *et al.* Microbiota and kidney disease: the road ahead. *Nature Reviews Nephrology* **21**, 702-716 (2025). https://doi.org/10.1038/s41581-025-00988-5

17 Chen, T. K., Knicely, D. H. & Grams, M. E. Chronic Kidney Disease Diagnosis and Management: A Review. *Jama* **322**, 1294-1304 (2019). https://doi.org/10.1001/jama.2019.14745

18 Patel, N., Yaqoob, M. M. & Aksentijevic, D. Cardiac metabolic remodelling in chronic kidney disease. *Nature Reviews Nephrology* **18**, 524-537 (2022). https://doi.org/10.1038/s41581-022-00576-x

19 Kaptoge, S. *et al.* C-reactive protein concentration and risk of coronary heart disease, stroke, and mortality: an individual participant meta-analysis. *Lancet* **375**, 132-140 (2010). https://doi.org/10.1016/s0140-6736(09)61717-7

20 Marques, F. Z., Mackay, C. R. & Kaye, D. M. Beyond gut feelings: how the gut microbiota regulates blood pressure. *Nature Reviews Cardiology* **15**, 20-32 (2018). https://doi.org/10.1038/nrcardio.2017.120

21 Avery, E. G. *et al.* Quantifying the impact of gut microbiota on inflammation and hypertensive organ damage. *Cardiovasc Res* **119**, 1441-1452 (2023). https://doi.org/10.1093/cvr/cvac121

22 Yang, B. H. *et al.* Foxp3+ T cells expressing RORγt represent a stable regulatory T-cell effector lineage with enhanced suppressive capacity during intestinal inflammation. *Mucosal Immunology* **9**, 444-457 (2016). https://doi.org/10.1038/mi.2015.74

23 Blatner, N. R. *et al.* Expression of RORγt marks a pathogenic regulatory T cell subset in human colon cancer. *Sci Transl Med* **4**, 164ra159 (2012). https://doi.org/10.1126/scitranslmed.3004566

24 Rothhammer, V. & Quintana, F. J. The aryl hydrocarbon receptor: an environmental sensor integrating immune responses in health and disease. *Nature reviews. Immunology* **19**, 184-197 (2019). https://doi.org/10.1038/s41577-019-0125-8

25 Quintana, F. J. *et al.* Control of T(reg) and T(H)17 cell differentiation by the aryl hydrocarbon receptor. *Nature* **453**, 65-71 (2008). https://doi.org/10.1038/nature06880

26 Veldhoen, M. *et al.* The aryl hydrocarbon receptor links TH17-cell-mediated autoimmunity to environmental toxins. *Nature* **453**, 106-109 (2008). https://doi.org/10.1038/nature06881

27 Delgobo, M. *et al.* Myocardial Milieu Favors Local Differentiation of Regulatory T Cells. *Circulation research* **132**, 565-582 (2023). https://doi.org/10.1161/CIRCRESAHA.122.322183

28 Hwang, S. J. *et al.* Indoxyl 3-sulfate stimulates Th17 differentiation enhancing phosphorylation of c-Src and STAT3 to worsen experimental autoimmune encephalomyelitis. *Toxicol Lett* **220**, 109-117 (2013). https://doi.org/10.1016/j.toxlet.2013.04.016

29 Schiattarella, G. G. *et al.* Nitrosative stress drives heart failure with preserved ejection fraction. *Nature* **568**, 351-356 (2019). https://doi.org/10.1038/s41586-019-1100-z

30 Bansal, N., Zelnick, L. R., Scherzer, R., Estrella, M. & Shlipak, M. G. Risk Factors and Outcomes Associated With Heart Failure With Preserved and Reduced Ejection Fraction in People With Chronic Kidney Disease. *Circulation. Heart failure* **17**, e011173 (2024). https://doi.org/10.1161/CIRCHEARTFAILURE.123.011173

31 Meijers, B. K. *et al.* p-Cresyl sulfate and indoxyl sulfate in hemodialysis patients. *Clin J Am Soc Nephrol* **4**, 1932-1938 (2009). https://doi.org/10.2215/cjn.02940509

1301 32 Kaesler, N. *et al.* Mapping cardiac remodeling in chronic kidney disease. *Sci Adv* **9**,
1302 eadj4846 (2023). https://doi.org/10.1126/sciadv.adj4846
1303 33 Naba, A. *et al.* The matrisome: in silico definition and in vivo characterization by
1304 proteomics of normal and tumor extracellular matrices. *Mol Cell Proteomics* **11**,
1305 M111.014647 (2012). https://doi.org/10.1074/mcp.M111.014647
1306 34 Patrick, R. *et al.* Integration mapping of cardiac fibroblast single-cell transcriptomes
1307 elucidates cellular principles of fibrosis in diverse pathologies. *Science Advances* **10**,
1308 eadk8501 (2024). https://doi.org/10.1126/sciadv.adk8501
1309 35 Barallobre-Barreiro, J. *et al.* Glycoproteomics Reveals Decorin Peptides With Anti-
1310 Myostatin Activity in Human Atrial Fibrillation. *Circulation* **134**, 817-832 (2016).
1311 https://doi.org/10.1161/CIRCULATIONAHA.115.016423
1312 36 Kober, C. *et al.* Targeting the aryl hydrocarbon receptor (AhR) with BAY 2416964: a
1313 selective small molecule inhibitor for cancer immunotherapy. *J Immunother Cancer*
1314 **11** (2023). https://doi.org/10.1136/jitc-2023-007495
1315 37 Kuppe, C. *et al.* Decoding myofibroblast origins in human kidney fibrosis. *Nature* **589**,
1316 281-286 (2021). https://doi.org/10.1038/s41586-020-2941-1
1317 38 Batra, G. *et al.* Interleukin 6 and Cardiovascular Outcomes in Patients With Chronic
1318 Kidney Disease and Chronic Coronary Syndrome. *JAMA Cardiol* **6**, 1440-1445 (2021).
1319 https://doi.org/10.1001/jamacardio.2021.3079
1320 39 Tonelli, M., Karumanchi, S. A. & Thadhani, R. Epidemiology and Mechanisms of
1321 Uremia-Related Cardiovascular Disease. *Circulation* **133**, 518-536 (2016).
1322 https://doi.org/doi:10.1161/CIRCULATIONAHA.115.018713
1323 40 Hayer, M. K. *et al.* Defining Myocardial Abnormalities Across the Stages of Chronic
1324 Kidney Disease: A Cardiac Magnetic Resonance Imaging Study. *JACC Cardiovasc*
1325 *Imaging* **13**, 2357-2367 (2020). https://doi.org/10.1016/j.jcmg.2020.04.021
1326 41 Bansal, N. *et al.* Burden and Outcomes of Heart Failure Hospitalizations in Adults
1327 With Chronic Kidney Disease. *Journal of the American College of Cardiology* **73**, 2691-
1328 2700 (2019). https://doi.org/10.1016/j.jacc.2019.02.071
1329 42 Schulman, G. *et al.* Randomized Placebo-Controlled EPPIC Trials of AST-120 in CKD.
1330 *Journal of the American Society of Nephrology : JASN* **26**, 1732-1746 (2015).
1331 https://doi.org/10.1681/ASN.2014010042
1332 43 Holle, J. *et al.* Inflammation in Children with CKD Linked to Gut Dysbiosis and
1333 Metabolite Imbalance. *J Am Soc Nephrol* **33**, 2259-2275 (2022).
1334 https://doi.org/10.1681/asn.2022030378
1335 44 Collett, J. A. *et al.* IL-17A Levels and Progression of Kidney Disease Following
1336 Hospitalization with and without Acute Kidney Injury. *Kidney360* **5**, 1623-1632
1337 (2024). https://doi.org/10.34067/kid.0000000000000559
1338 45 Kimura, A., Naka, T., Nohara, K., Fujii-Kuriyama, Y. & Kishimoto, T. Aryl hydrocarbon
1339 receptor regulates Stat1 activation and participates in the development of Th17
1340 cells. *Proceedings of the National Academy of Sciences* **105**, 9721-9726 (2008).
1341 https://doi.org/doi:10.1073/pnas.0804231105
1342 46 Schroeder, J. C. *et al.* The uremic toxin 3-indoxyl sulfate is a potent endogenous
1343 agonist for the human aryl hydrocarbon receptor. *Biochemistry* **49**, 393-400 (2010).
1344 https://doi.org/10.1021/bi901786x
1345 47 Kaminski, T. W., Pawlak, K., Karbowska, M., Mysliwiec, M. & Pawlak, D. Indoxyl
1346 sulfate - the uremic toxin linking hemostatic system disturbances with the

prevalence of cardiovascular disease in patients with chronic kidney disease. *BMC Nephrol* **18**, 35 (2017). https://doi.org/10.1186/s12882-017-0457-1

48 Lochner, M. *et al.* In vivo equilibrium of proinflammatory IL-17+ and regulatory IL-10+ Foxp3+ RORgamma t+ T cells. *The Journal of experimental medicine* **205**, 1381-1393 (2008). https://doi.org/10.1084/jem.20080034

49 Kim, M. J. *et al.* Deletion of PD-1 destabilizes the lineage identity and metabolic fitness of tumor-infiltrating regulatory T cells. *Nature immunology* **24**, 148-161 (2023). https://doi.org/10.1038/s41590-022-01373-1

50 Cortes, J. R. *et al.* Maintenance of immune tolerance by Foxp3+ regulatory T cells requires CD69 expression. *Journal of autoimmunity* **55**, 51-62 (2014). https://doi.org/10.1016/j.jaut.2014.05.007

51 Ichikawa, T. *et al.* CD103(hi) T(reg) cells constrain lung fibrosis induced by CD103(lo) tissue-resident pathogenic CD4 T cells. *Nature immunology* **20**, 1469-1480 (2019). https://doi.org/10.1038/s41590-019-0494-y

52 Mantovani, A., Cassatella, M. A., Costantini, C. & Jaillon, S. Neutrophils in the activation and regulation of innate and adaptive immunity. *Nature Reviews Immunology* **11**, 519-531 (2011). https://doi.org/10.1038/nri3024

53 Stark, M. A. *et al.* Phagocytosis of Apoptotic Neutrophils Regulates Granulopoiesis via IL-23 and IL-17. *Immunity* **22**, 285-294 (2005). https://doi.org/https://doi.org/10.1016/j.immuni.2005.01.011

54 Wilson, A. S. *et al.* Neutrophil extracellular traps and their histones promote Th17 cell differentiation directly via TLR2. *Nature Communications* **13**, 528 (2022). https://doi.org/10.1038/s41467-022-28172-4

55 Valente, A. J. *et al.* Interleukin-17A stimulates cardiac fibroblast proliferation and migration via negative regulation of the dual-specificity phosphatase MKP-1/DUSP-1. *Cellular Signalling* **24**, 560-568 (2012). https://doi.org/https://doi.org/10.1016/j.cellsig.2011.10.010

56 Wu, L. *et al.* Cardiac fibroblasts mediate IL-17A-driven inflammatory dilated cardiomyopathy. *The Journal of experimental medicine* **211**, 1449-1464 (2014). https://doi.org/10.1084/jem.20132126

57 Träger, C. *et al.* A probiotic approach identifies a Treg-centred immunoregulation via modulation of gut microbiota metabolites in people with multiple sclerosis and healthy individuals. *EBioMedicine* **116**, 105743 (2025). https://doi.org/10.1016/j.ebiom.2025.105743

58 Thiele, A. *et al.* Pharmacological inhibition of adipose tissue adipose triglyceride lipase by Atglistatin prevents catecholamine-induced myocardial damage. *Cardiovasc Res* **118**, 2488-2505 (2022). https://doi.org/10.1093/cvr/cvab182

59 Beyhoff, N. *et al.* Application of Speckle-Tracking Echocardiography in an Experimental Model of Isolated Subendocardial Damage. *J Am Soc Echocardiogr* **30**, 1239-1250.e1232 (2017). https://doi.org/10.1016/j.echo.2017.08.006

60 Sadik, A. *et al.* IL4I1 Is a Metabolic Immune Checkpoint that Activates the AHR and Promotes Tumor Progression. *Cell* **182**, 1252-1270.e1234 (2020). https://doi.org/10.1016/j.cell.2020.07.038

61 Finak, G. *et al.* MAST: a flexible statistical framework for assessing transcriptional changes and characterizing heterogeneity in single-cell RNA sequencing data. *Genome Biology* **16**, 278 (2015). https://doi.org/10.1186/s13059-015-0844-5

62 Cui, A. *et al.* Dictionary of immune responses to cytokines at single-cell resolution. *Nature* **625**, 377-384 (2024). https://doi.org/10.1038/s41586-023-06816-9

63 Versnjak, J. *et al.* Deep phenotyping of heart failure with preserved ejection fraction through multi-omics integration. *Eur J Heart Fail* (2025). https://doi.org/10.1002/ejhf.70041

1399 **Figure Legends**

1400 **Figure 1. Depletion of microbiome-derived metabolites attenuates cardiac**
1401 **remodeling in mice with impaired kidney function. (a)** 129/Sv mice were
1402 randomized to receive a broad-spectrum, oral antibiotic cocktail (Abx) or control
1403 drinking water. After one week, mice underwent two-stage subtotal nephrectomy
1404 (STNx) or sham surgery. **(b)** Representative ^{1}H-NMR plasma spectra 13 weeks after
1405 surgery and **(c)** quantification of the aromatic region, normalized to the respective
1406 sham group. **(d)** Heatmap of plasma metabolites quantified by liquid chromatography-
1407 mass spectrometry (LC-MS). **(e)** Plasma concentrations of sulfated microbiome-
1408 derived metabolites quantified by LC-MS. Transdermal glomerular filtration rate (GFR)
1409 normalized measured **(f)** longitudinally and **(g)** at endpoint. **(h)** Heart weight
1410 normalized to tibia length at the endpoint. **(i)** Representative echocardiographic
1411 images at the endpoint. **(j)** Left ventricular posterior wall thickness at end-diastole
1412 (LVPWd). **(k)** Longitudinal changes in normalized left ventricular (LV) mass. **(l)**
1413 Ejection fraction (EF), **(m)** E/e′ ratio, **(n)** global longitudinal strain (GLS) at the
1414 endpoint. **(o)** Histological assessment of left ventricular fibrosis by Sirius Red staining
1415 (scale bars: upper, 1 mm; lower, 100 μm) and **(p)** quantification of fibrotic area. **(q)**
1416 Quantification of leukocytes in the heart at the endpoint by flow cytometry. **(r)** Plasma
1417 C-reactive protein (CRP) levels at the endpoint. **(s)** Radiotelemetric blood pressure
1418 (BP) measurement. **(t)** Representative average systolic BP (SBP) plots at baseline
1419 (week 0) and week 12, and **(u)** quantification. **(v)** Acetylcholine (ACh)-induced
1420 endothelial-dependent vasorelaxation of mesenteric arteries assessed by wire
1421 myography, and **(w)** corresponding EC_{50} values. Symbols in **(f)** and **(k)** indicate the
1422 following comparisons: Sham vs. STNx (‡), Sham Abx vs. STNx Abx (#), and STNx
1423 vs. STNx Abx (*). Data are shown as mean ± SEM. Each dot represents one mouse.
1424 Statistical analyses were performed using one-way ANOVA or Kruskal-Wallis test
1425 followed by Tukey's or Dunn's *post hoc* correction, as appropriate, unless otherwise
1426 indicated. Mann Whitney U-tests with false discovery rate correction according to
1427 Benjamini-Hochberg were used for metabolomics data. Two-group comparisons for
1428 the aromatic NMR region **(c)** and EC_{50} values **(w)** were performed using unpaired two-
1429 tailed Student's t test. Two-group comparisons of systolic blood pressure in **(u)** were
1430 assessed by Mann–Whitney U test.

1431

1432 **Figure 2. Kidney disease induces microbiota-dependent Th17-driven systemic**
1433 **and cardiac inflammation.** Immune cells were isolated from spleens and analyzed
1434 by flow cytometry. **(a)** Abundance of neutrophils ($CD45^+$ $CD3^-$ $NK1.1^-$ $CD11b^+$ $Ly6G^+$)
1435 among $CD45^+$ cells. **(b)** Ratio of T helper (T_H, $CD45^+$ $CD3^+$ $TCR\gamma\delta^-$ $CD4^+$ $CD8^-$) to
1436 cytotoxic T cells (T_C, $CD45^+$ $CD3^+$ $TCR\gamma\delta^-$ $CD4^+$ $CD8^-$). **(c)** UMAP projection of splenic
1437 T cell populations based on flow cytometry. **(d)** Frequencies of effector memory (EM,
1438 $CD44^+$ $CD62L^-$) conventional T cells (T_{conv}, $FoxP3^-$ T_H). **(e)** Frequencies of EM
1439 regulatory T cells (T_{reg}, $FoxP3^+$ T_H). **(f)** Frequencies of $ROR\gamma t^+$ T_{conv}. **(g)** Changes in
1440 $ROR\gamma t^+$ T_{conv} abundance between experimental groups
1441 (* p-adj. < 0.1). **(h)** Frequencies of $ROR\gamma t^+$ T_{reg}. **(i)** Longitudinal frequencies of $ROR\gamma t^+$
1442 T_{conv} (left) and T_{reg} (right). **(j)** Aryl hydrocarbon receptor (AhR) activation of plasma in
1443 reporter cell line. **(k)** *Cyp1a1* expression in splenocytes. **(l)** Representative flow
1444 cytometric plots of cardiac $ROR\gamma t^+$ T_{reg} ($T_{reg}17$) and **(m)** quantification. **(n)** Overlap of
1445 differentially expressed genes (DEG) in cardiac bulk mRNA-sequencing between the
1446 two indicated comparisons. **(o)** Significantly enriched biological pathways in the
1447 cardiac transcriptome. **(p)** Targeted gene ontology (GO) and pathway analysis of IL-
1448 17A-related differentially enriched gene sets. Data are shown as mean ± SEM. Each
1449 dot represents one mouse. Statistical analyses were performed using one-way
1450 ANOVA or Kruskal-Wallis test followed by Tukey's or Dunn's *post hoc* correction, as
1451 appropriate, unless otherwise indicated. For (g), Benjamini-Hochberg false discovery
1452 rate (FDR) correction was performed. For RNA sequencing, DEG were generated
1453 using the DeSeq2 pipeline with appropriate FDR correction. Gene set enrichment
1454 analyses were performed using Fisher's exact test followed by FDR correction.

1455

1456 **Figure 3. Indoxyl sulfate induces inflammation and cardiac fibrosis independent**
1457 **of kidney function. (a, b)** *In vitro* T_H17 differentiation of naïve T helper cells from
1458 129/Sv mice in the presence and absence of indoxyl sulfate (IxS). Two biological
1459 replicates, three technical replicates each. **(c)** Heart failure with preserved ejection
1460 fraction was induced in 129/Sv mice using high-fat diet (HFD) and L-NAME in the
1461 drinking water for 15 weeks. Mice received either IxS or potassium chloride (KCl,
1462 control) in the drinking water throughout the experiment. **(d)** Plasma IxS measured by
1463 liquid chromatography-mass spectrometry (LC-MS). **(e)** Plasma cystatin C levels. (f)
1464 *Cyp1a1* expression in spleen. Flow cytometric quantification of IL17A in splenic **(g)**

1465 T_{conv} ($CD45^+$ $CD3^+$ $TCR\gamma\delta^-$ $CD4^+$ $CD8^-$ $FoxP3^-$) and **(h)** T_{reg} ($CD45^+$ $CD3^+$ $TCR\gamma\delta^-$
1466 $CD4^+$ $CD8^-$ $FoxP3^+$). **(i)** Heart weight normalized to tibia length. **(j)** Cardiac interstitial
1467 fibrosis, assessed by histological staining for collagen type I (COL-1) and fibronectin
1468 (FN-1) (scale bar: 100 µm), with quantification of **(k)** FN-1 and **(l)** COL-1. Data are
1469 shown as mean ± SEM. Each dot represents one mouse. Statistical analyses were
1470 performed using one-tailed Student's t test or Mann-Whitney U-test, as appropriate.
1471 **(b)** Statistical analysis was performed using linear regression.

1472

1473 **Figure 4. IL-17A-signaling in IxS-primed cardiac fibroblasts promotes**
1474 **extracellular matrix production.** Cardiac *Il17ra* expression in **(a)** 129/Sv mice
1475 subjected to subtotal nephrectomy (STNx) or sham operation and treated with either
1476 an antibiotic cocktail (Abx) or control drinking water, and in **(b)** 129/Sv mice subjected
1477 to high-fat diet (HFD) plus L-NAME and indoxyl sulfate (IxS) or potassium chloride
1478 (KCl, control) in the drinking water. Re-analysis of previously published cardiac single
1479 nuclei (sn) RNA-sequencing data (Kaesler *et al.*) from STNx mice shows **(c)** highest
1480 *Il17ra* expression in fibroblasts and **(d)** higher extracellular matrix (ECM) gene set
1481 score in *Il17ra* expressing cardiac fibroblasts. **(e)** Enrichment analysis for known
1482 cardiac fibroblasts subtypes within differentially expressed genes. **(f)** Cardiac
1483 fibroblasts were isolated from C57BL/6J mice for *ex vivo* treatment with IxS and IL-
1484 17A. Purity validation **(g)** by histology using platelet-derived growth factor receptor
1485 alpha (PDGFRA) and vimentin (VIM) (scale bar: 100 µm), and **(h)** by flow cytometry
1486 showing $CD45^-$ $CD31^-$ $PDGFRA^+$ fibroblasts. **(i)** *Il17ra* expression following *in vitro*
1487 incubation with IxS. Isolated fibroblasts were incubated with 100µM IxS, 1ng/mL IL-
1488 17A, or both and expression of **(j)** *Col1a1*, **(k)** *Col1a2*, **(l)** *Acta2*, **(m)** *Abi3bp* were
1489 quantified. **(n)** Histological confirmation of IL-17RA expression in cardiac fibroblasts
1490 (scale bar: 100 µm). **(a, b)** Data are shown as mean ± SEM. Each dot represents one
1491 mouse. **(i-m)** Data are combined from four biological replicates, with three technical
1492 replicates each. Statistical analyses were performed using one-way ANOVA or
1493 Kruskal-Wallis test followed by Tukey's or Dunn's *post hoc* correction, as appropriate.
1494 **(b)** Statistical analysis was performed using one-tailed Student's t test. **(d)** Comparison
1495 by two-sided Mann-Whitney U-test.

1496

1497 **Figure 5. Pharmacological blockade of the AhR ameliorates inflammation and**
1498 **cardiac remodeling in kidney disease. (a)** *Ex vivo* aryl hydrocarbon receptor (AhR)
1499 inhibition in immune cells from 129/Sv mice with BAY 2416964 (AhRi). **(b)** AhRi blocks
1500 indoxyl sulfate (IxS)-induced *Cyp1a1* gene expression in splenocytes. **(c)** AhRi
1501 suppresses IxS-enhanced TH17 differentiation of naïve T cells. **(d)** 129/Sv mice
1502 underwent two stage subtotal nephrectomy (STNx) or sham surgery. Two weeks after
1503 completion of surgery, STNx mice were randomized to AhRi or vehicle (VEH)
1504 treatment based on plasma cystatin C. **(e)** Survival analysis according to pre-specified
1505 humane endpoints. **(f)** Plasma C-reactive protein (CRP) levels. **(g)** *Cyp1a1* expression
1506 in splenocytes. RORγt in splenic **(h)** T_{conv} ($CD45^+$ $CD3^+$ $TCR\gamma\delta^-$ $CD4^+$ $CD8^-$ $FoxP3^-$)
1507 and **(i)** T_{reg} ($CD45^+$ $CD3^+$ $TCR\gamma\delta^-$ $CD4^+$ $CD8^-$ $FoxP3^+$) by flow cytometry. **(j)** Left
1508 ventricular (LV) mass normalized to tibia length, **(i)** E/e' ratio and **(l)** global longitudinal
1509 strain (GLS) from endpoint echocardiography. **(m)** Cardiac fibrosis assessed by Sirius
1510 Red staining (scale bar top: 1mm, bottom: 100µm). **(n)** Quantification of Sirius Red-
1511 positive interstitial fibrosis. **(o)** Cardiac *Il17ra* expression. **(p)** Enriched biological
1512 pathways among differentially expressed genes significant in STNx rescued by AhRi.
1513 **(q)** Targeted gene ontology (GO) analysis of IL-17A-related differentially expressed
1514 gene sets. **(b-c)** Data are combined from three technical replicates. **(c)** Data were
1515 analyzed by nonlinear sigmoidal regression. **(e-o)** Data are shown as mean ± SEM.
1516 Each dot represents one mouse. Statistical analyses were performed using one-way
1517 ANOVA or Kruskal-Wallis test followed by Tukey's or Dunn's *post hoc* correction, as
1518 appropriate, unless otherwise indicated. Gene set enrichment analyses were
1519 performed using Fisher's exact test.

1520

1521 **Figure 6. Validation of the pro-fibrotic AhR-IL-17A axis in patients with chronic**
1522 **kidney disease. (a)** Activation of aryl hydrocarbon receptor (AhR) in HT29-Lucia AhR
1523 reporter cells with 100µM indoxyl sulfate (IxS) is blockable by the AhR inhibitor BAY
1524 2416964 (AhRi). **(b)** Serum was obtained from healthy controls (HC) or patients with
1525 chronic kidney disease treated with hemodialysis (HD) for *in vitro* testing on AhR
1526 reporter and naïve T cells. **(c)** Activation of the AhR in response to HC or HD serum
1527 in the presence or absence of AhRi. **(d)** *In vitro* T_H17 differentiation of naïve T cells
1528 from healthy volunteers in the presence of HC and HD serum. **(e)** Plasma IL-17A
1529 derived from OLINK Explore HT in the UK Biobank (UKBB) stratified by estimated

1530 glomerular filtration rate (eGFR) and albuminuria in patients with available data.
1531 Statistical comparisons are made between the reference cell (G1, A1) and each
1532 corresponding cell. Adjusted p-values indicate significance as follows: *** < 0.001,
1533 ** < 0.01, * < 0.05. **(f)** Plasma IL-17A in patients with CKD defined by an eGFR < 60
1534 mL/min/1.73 m². with and without heart failure with persevered ejection fraction
1535 (HFpEF). **(g)** Kaplan-Meier survival curves for all-cause mortality stratified by IL-17A
1536 levels (<25th, 25th -75th, >75th percentile) among participants with eGFR < 60
1537 mL/min/1.73 m². **(h)** Corresponding hazard ratios and 95% confidence intervals from
1538 a Cox proportional hazards model for all-cause mortality. Model 1 only IL-17A. Model
1539 2 additionally adjusted for age, sex, and eGFR. Model 3 further adjusted for
1540 hypertension, diabetes, pack years, BMI, and NT-proBNP. **(i)** Human primary cardiac
1541 fibroblasts were incubated *in vitro* with HC and HD serum in addition of anti-IL-17A
1542 (Secukinumab, αIL17A) or AhRi and analyzed for **(j)** *IL17RA*, **(k)** *COL1A1*, **(l)** *COL1A2*,
1543 and **(m)** *ACTA2* expression. **(a, c)** Data are combined from three biological replicates,
1544 with three technical replicates each and **(h-k)** data combined from two primary cell
1545 lines from different donors treated with HC serum (n = 4 donors) or HD serum (n = 9
1546 donors) in triplicates. Statistical analyses were performed using one-way ANOVA or
1547 Kruskal-Wallis test followed by Tukey's or Dunn's *post hoc* correction, as appropriate.

Figure 1

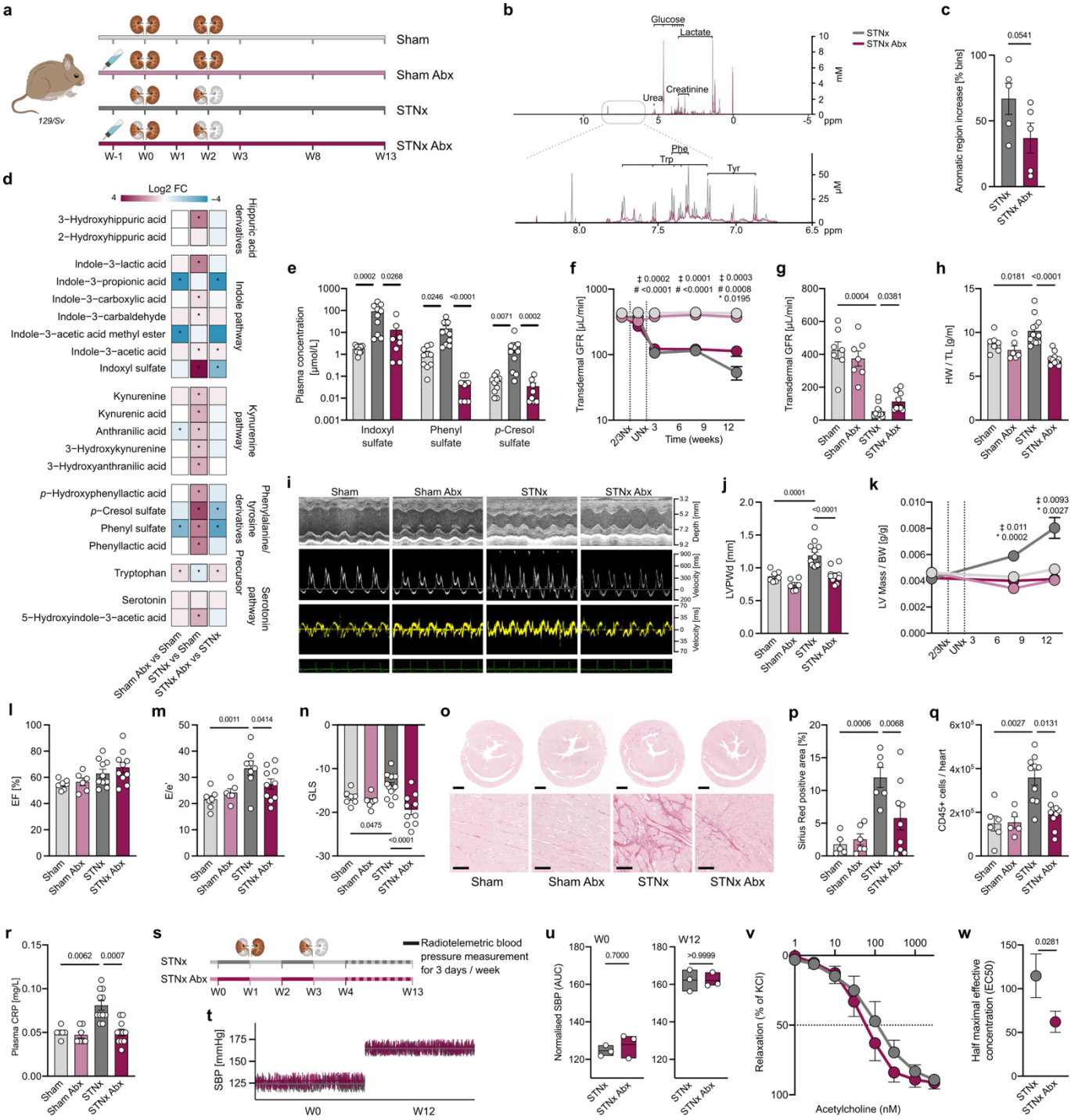
a
129/Sv
Sham
Sham Abx
STNx
STNx Abx
W-1
W0
W1
W2
W3
W8
W13
b
Glucose
Lactate
Creatinine
Urea
STNx
STNx Abx
mM
ppm
Phe
Trp
Tyr
µM
c
Aromatic region increase [% bins]
0.0541
d
Log2 FC
Hippuric acid derivatives
3−Hydroxyhippuric acid
2−Hydroxyhippuric acid
Indole pathway
Indole−3−lactic acid
Indole−3−propionic acid
Indole−3−carboxylic acid
Indole−3−carbaldehyde
Indole−3−acetic acid methyl ester
Indole−3−acetic acid
Indoxyl sulfate
Kynurenine pathway
Kynurenine
Kynurenic acid
Anthranilic acid
3−Hydroxykynurenine
3−Hydroxyanthranilic acid
Phenylalanine/tyrosine derivatives
p−Hydroxyphenyllactic acid
p−Cresol sulfate
Phenyl sulfate
Phenyllactic acid
Precursor
Tryptophan
Serotonin pathway
Serotonin
5−Hydroxyindole−3−acetic acid
Sham Abx vs Sham
STNx vs Sham
STNx Abx vs STNx
e
Plasma concentration [µmol/L]
Indoxyl sulfate
Phenyl sulfate
p-Cresol sulfate
f
Transdermal GFR [µL/min]
Time (weeks)
2/3Nx
UNx
g
Transdermal GFR [µL/min]
h
HW / TL [g/m]
i
Sham
Sham Abx
STNx
STNx Abx
Depth [mm]
Velocity [ms]
j
LVPWd [mm]
k
LV Mass / BW [g/g]
l
EF [%]
m
E/e'
n
GLS
o
Sham
Sham Abx
STNx
STNx Abx
p
Sirius Red positive area [%]
q
CD45+ cells / heart
r
Plasma CRP [mg/L]
s
STNx
STNx Abx
Radiotelemetric blood pressure measurement for 3 days / week
W0
W1
W2
W3
W4
W13
t
SBP [mmHg]
W0
W12
u
Normalised SBP (AUC)
W0
W12
0.7000
>0.9999
v
Relaxation (% of KCl)
Acetylcholine (nM)
w
Half maximal effective concentration (EC50)
0.0281

Figure 2

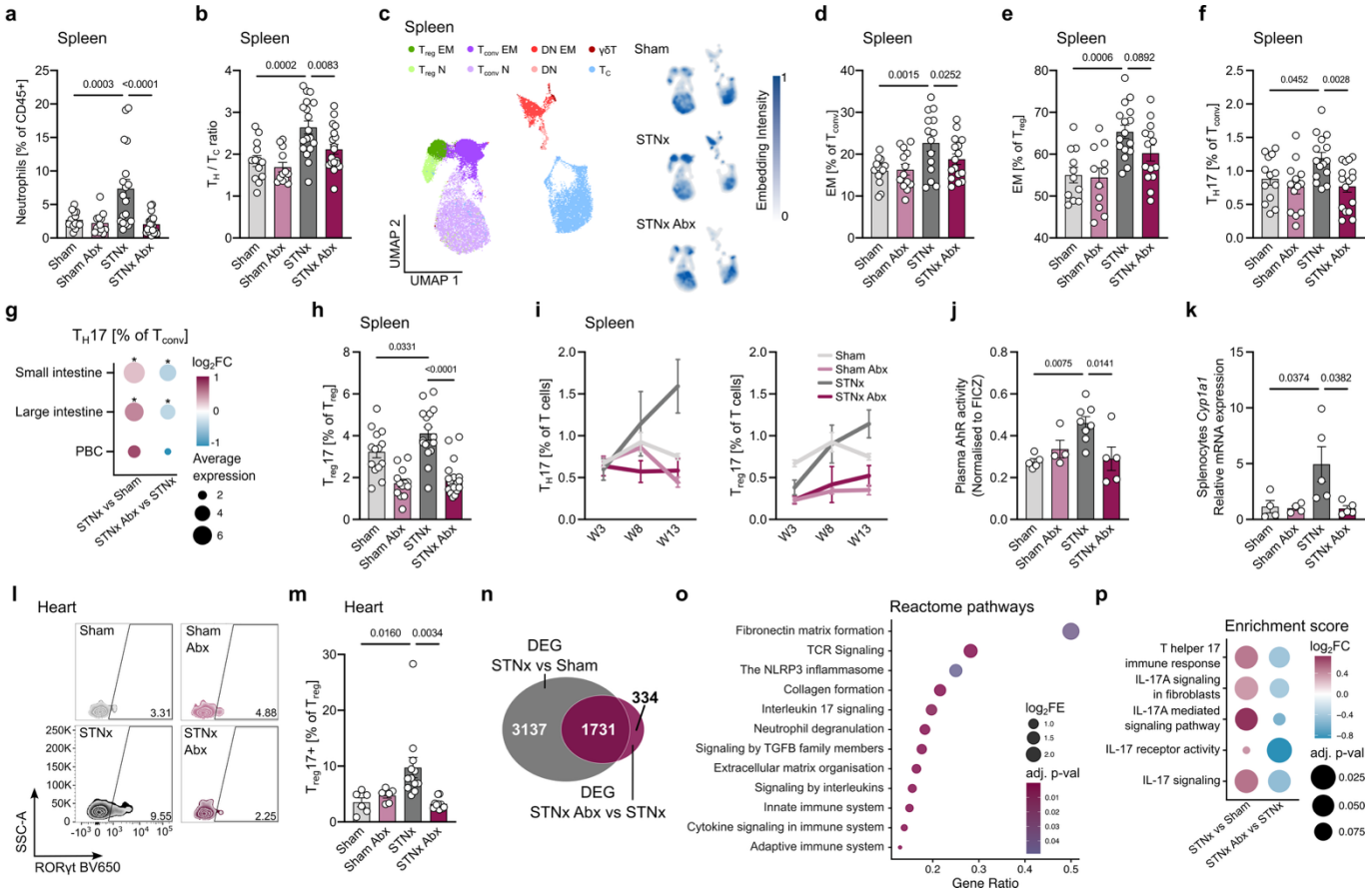
a
Spleen
Neutrophils [% of CD45+]
0.0003
<0.0001
Sham
Sham Abx
STNx
STNx Abx
b
Spleen
T_H / T_C ratio
0.0002
0.0083
c
Spleen
T_{reg} EM
T_{conv} EM
DN EM
γδT
T_{reg} N
T_{conv} N
DN
T_C
UMAP 1
UMAP 2
Sham
STNx
STNx Abx
Embedding Intensity
d
Spleen
EM [% of T_{conv}]
0.0015
0.0252
e
Spleen
EM [% of T_{reg}]
0.0006
0.0892
f
Spleen
T_H17 [% of T_{conv}]
0.0452
0.0028
g
T_H17 [% of T_{conv}]
Small intestine
Large intestine
PBC
STNx vs Sham
STNx Abx vs STNx
log_2FC
Average expression
h
Spleen
$T_{reg}17$ [% of T_{reg}]
0.0331
<0.0001
i
Spleen
T_H17 [% of T cells]
$T_{reg}17$ [% of T cells]
W3
W8
W13
j
Plasma AhR activity (Normalised to FICZ)
0.0075
0.0141
k
Splenocytes *Cyp1a1* Relative mRNA expression
0.0374
0.0382
l
Heart
Sham
Sham Abx
STNx
STNx Abx
3.31
4.88
9.55
2.25
SSC-A
RORγt BV650
m
Heart
$T_{reg}17+$ [% of T_{reg}]
0.0160
0.0034
n
DEG
STNx vs Sham
3137
1731
334
DEG
STNx Abx vs STNx
o
Reactome pathways
Fibronectin matrix formation
TCR Signaling
The NLRP3 inflammasome
Collagen formation
Interleukin 17 signaling
Neutrophil degranulation
Signaling by TGFB family members
Extracellular matrix organisation
Signaling by interleukins
Innate immune system
Cytokine signaling in immune system
Adaptive immune system
Gene Ratio
log_2FE
adj. p-val
p
Enrichment score
T helper 17 immune response
IL-17A signaling in fibroblasts
IL-17A mediated signaling pathway
IL-17 receptor activity
IL-17 signaling
STNx vs Sham
STNx Abx vs STNx
log_2FC
adj. p-val

Figure 3

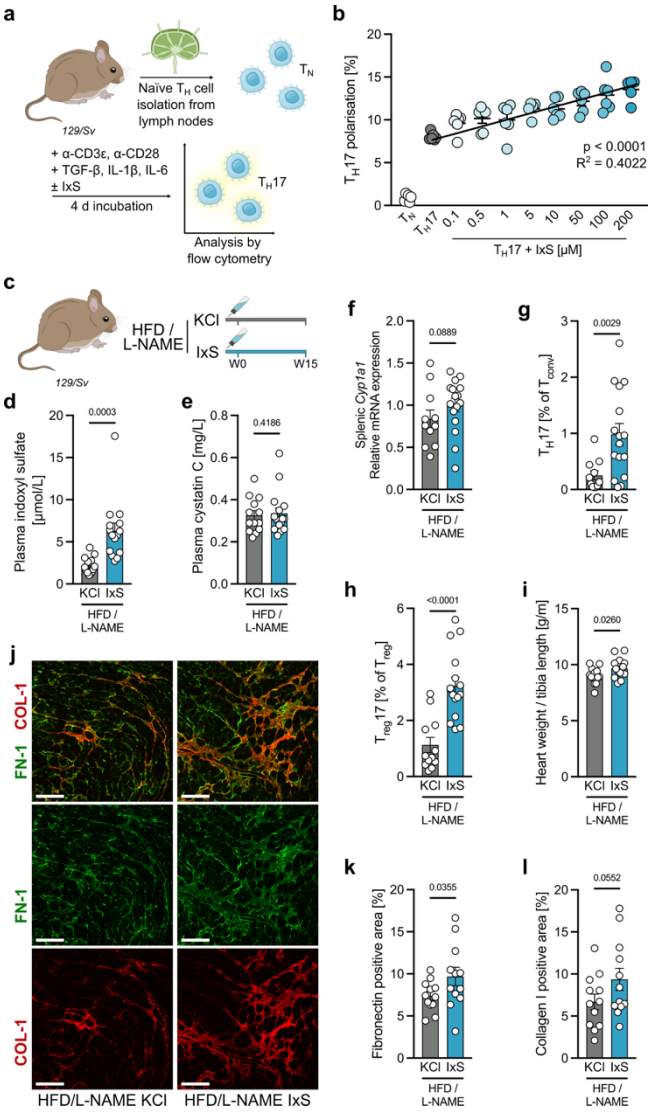
a
129/Sv
Naïve T_H cell isolation from lymph nodes
T_N
+ α-CD3ε, α-CD28
+ TGF-β, IL-1β, IL-6
± IxS
4 d incubation
T_H17
Analysis by flow cytometry
b
T_H17 polarisation [%]
p < 0.0001
R^2 = 0.4022
T_H17 + IxS [μM]
c
HFD / L-NAME
KCl
IxS
W0
W15
d
Plasma indoxyl sulfate [μmol/L]
0.0003
e
Plasma cystatin C [mg/L]
0.4186
f
Splenic Cyp1a1 Relative mRNA expression
0.0889
g
T_H17 [% of T_{conv}]
0.0029
h
$T_{reg}17$ [% of T_{reg}]
<0.0001
i
Heart weight / tibia length [g/m]
0.0260
j
COL-1
FN-1
FN-1
COL-1
HFD/L-NAME KCl
HFD/L-NAME IxS
k
Fibronectin positive area [%]
0.0355
l
Collagen I positive area [%]
0.0552

Figure 4

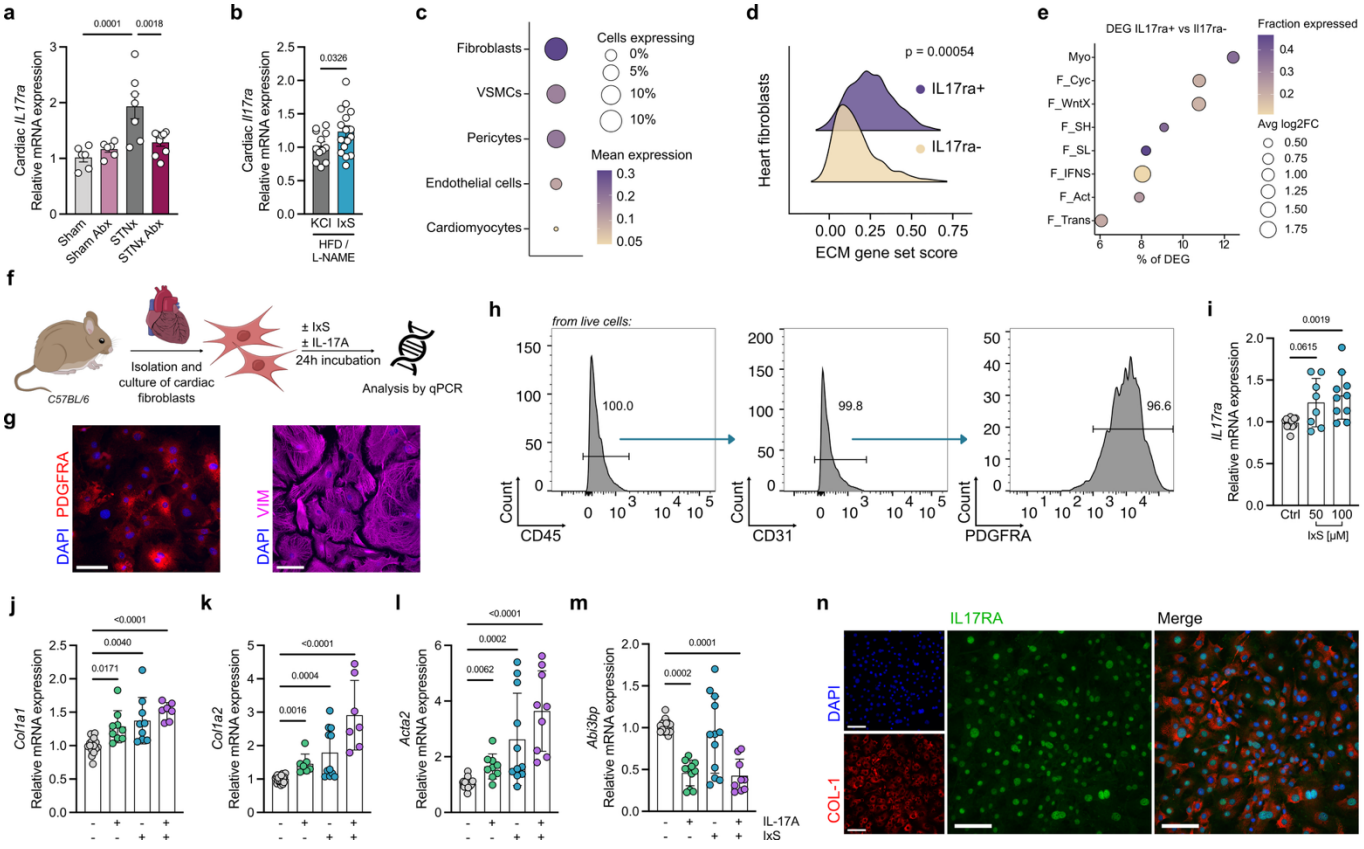
a
Cardiac IL17ra
Relative mRNA expression
0.0001
0.0018
Sham
Sham Abx
STNx
STNx Abx
b
Cardiac Il17ra
Relative mRNA expression
0.0326
KCl
IxS
HFD / L-NAME
c
Fibroblasts
VSMCs
Pericytes
Endothelial cells
Cardiomyocytes
Cells expressing
0%
5%
10%
10%
Mean expression
0.3
0.2
0.1
0.05
d
Heart fibroblasts
p = 0.00054
IL17ra+
IL17ra-
ECM gene set score
e
DEG IL17ra+ vs Il17ra-
Fraction expressed
Avg log2FC
Myo
F_Cyc
F_WntX
F_SH
F_SL
F_IFNS
F_Act
F_Trans
% of DEG
f
C57BL/6
Isolation and culture of cardiac fibroblasts
± IxS
± IL-17A
24h incubation
Analysis by qPCR
g
DAPI PDGFRA
DAPI VIM
h
from live cells:
100.0
99.8
96.6
Count
CD45
CD31
PDGFRA
i
IL17ra
Relative mRNA expression
0.0019
0.0615
Ctrl
50
100
IxS [µM]
j
Col1a1
Relative mRNA expression
<0.0001
0.0040
0.0171
k
Col1a2
Relative mRNA expression
<0.0001
0.0004
0.0016
l
Acta2
Relative mRNA expression
<0.0001
0.0002
0.0062
m
Abi3bp
Relative mRNA expression
0.0001
0.0002
IL-17A
IxS
n
IL17RA
Merge
DAPI
COL-1

Figure 5

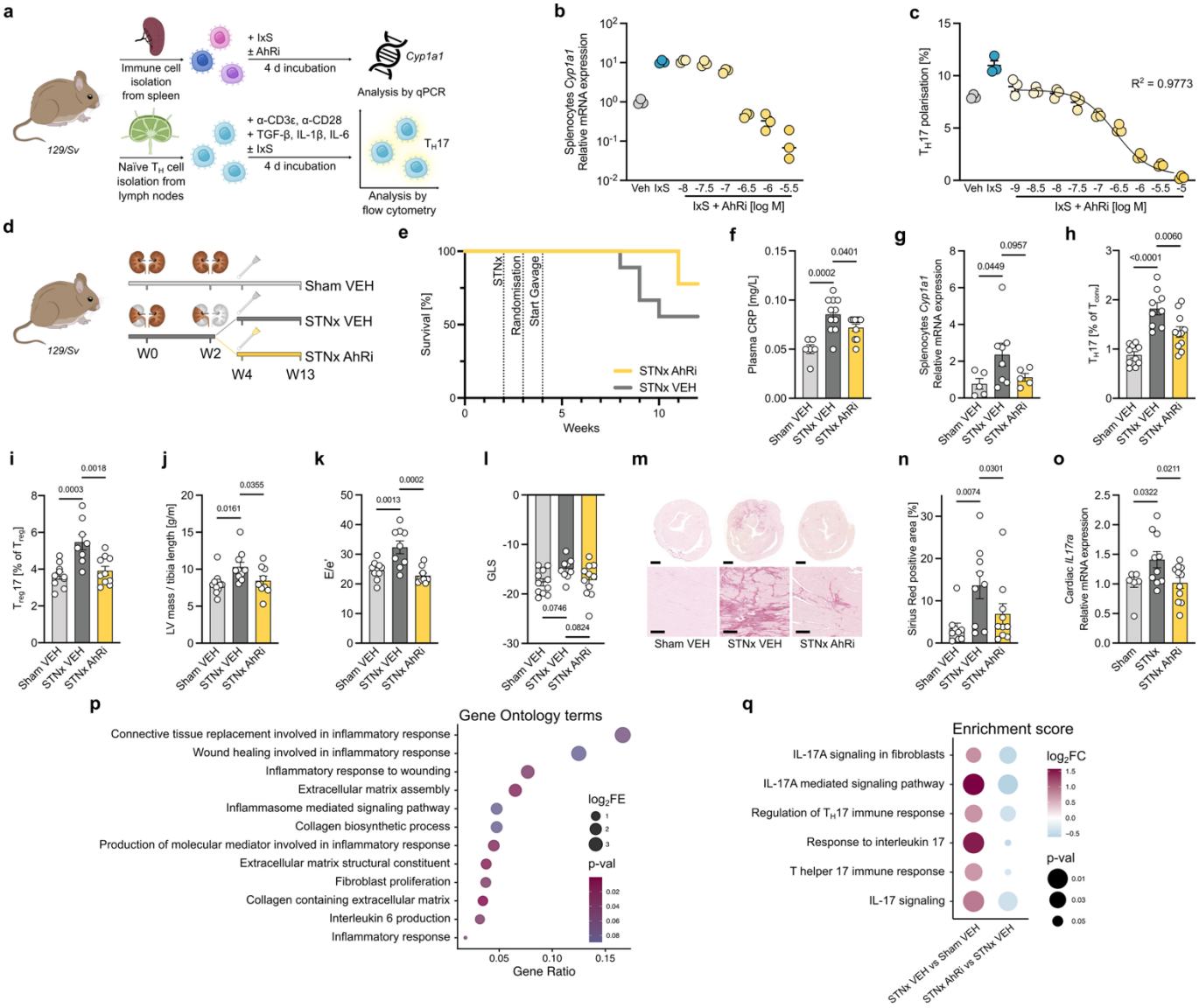
a
129/Sv
Immune cell isolation from spleen
+ IxS
± AhRi
4 d incubation
Cyp1a1
Analysis by qPCR
Naïve T_H cell isolation from lymph nodes
+ α-CD3ε, α-CD28
+ TGF-β, IL-1β, IL-6
± IxS
4 d incubation
T_H17
Analysis by flow cytometry
b
Splenocytes Cyp1a1 Relative mRNA expression
Veh IxS -8 -7.5 -7 -6.5 -6 -5.5
IxS + AhRi [log M]
c
T_H17 polarisation [%]
R^2 = 0.9773
Veh IxS -9 -8.5 -8 -7.5 -7 -6.5 -6 -5.5 -5
IxS + AhRi [log M]
d
129/Sv
Sham VEH
STNx VEH
STNx AhRi
W0
W2
W4
W13
e
Survival [%]
STNx
Randomisation
Start Gavage
STNx AhRi
STNx VEH
Weeks
f
Plasma CRP [mg/L]
0.0002
0.0401
g
Splenocytes Cyp1a1 Relative mRNA expression
0.0449
0.0957
h
T_H17 [% of T_{conv}]
<0.0001
0.0060
i
$T_{reg}17$ [% of T_{reg}]
0.0003
0.0018
j
LV mass / tibia length [g/m]
0.0161
0.0355
k
E/e'
0.0013
0.0002
l
GLS
0.0746
0.0824
m
Sham VEH
STNx VEH
STNx AhRi
n
Sirius Red positive area [%]
0.0074
0.0301
o
Cardiac IL17ra Relative mRNA expression
0.0322
0.0211
Sham VEH
STNx VEH
STNx AhRi
Sham
STNx
p
Gene Ontology terms
Connective tissue replacement involved in inflammatory response
Wound healing involved in inflammatory response
Inflammatory response to wounding
Extracellular matrix assembly
Inflammasome mediated signaling pathway
Collagen biosynthetic process
Production of molecular mediator involved in inflammatory response
Extracellular matrix structural constituent
Fibroblast proliferation
Collagen containing extracellular matrix
Interleukin 6 production
Inflammatory response
log2FE
p-val
Gene Ratio
q
Enrichment score
IL-17A signaling in fibroblasts
IL-17A mediated signaling pathway
Regulation of T_H17 immune response
Response to interleukin 17
T helper 17 immune response
IL-17 signaling
log2FC
p-val
STNx VEH vs Sham VEH
STNx AhRi vs STNx VEH

Figure 6

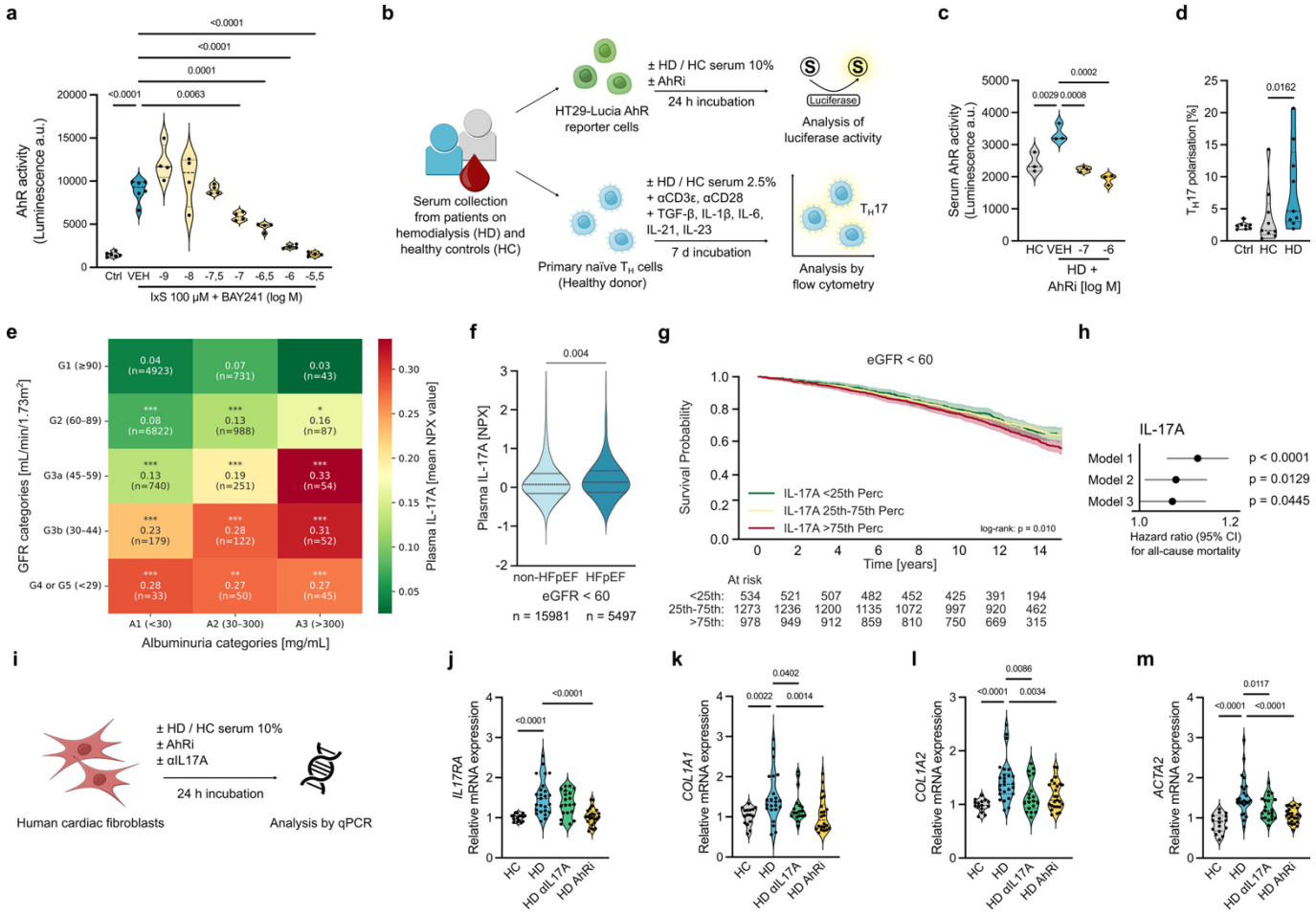
a
AhR activity (Luminescence a.u.)
Ctrl VEH -9 -8 -7,5 -7 -6,5 -6 -5,5
IxS 100 µM + BAY241 (log M)
b
Serum collection from patients on hemodialysis (HD) and healthy controls (HC)
HT29-Lucia AhR reporter cells
± HD / HC serum 10%
± AhRi
24 h incubation
Luciferase
Analysis of luciferase activity
Primary naïve TH cells (Healthy donor)
± HD / HC serum 2.5%
+ αCD3ε, αCD28
+ TGF-β, IL-1β, IL-6, IL-21, IL-23
7 d incubation
TH17
Analysis by flow cytometry
c
Serum AhR activity (Luminescence a.u.)
HC VEH -7 -6
HD + AhRi [log M]
d
TH17 polarisation [%]
Ctrl HC HD
e
GFR categories [mL/min/1.73m²]
G1 (≥90)
G2 (60-89)
G3a (45-59)
G3b (30-44)
G4 or G5 (<29)
A1 (<30) A2 (30-300) A3 (>300)
Albuminuria categories [mg/mL]
Plasma IL-17A [mean NPX value]
f
Plasma IL-17A [NPX]
non-HFpEF HFpEF
eGFR < 60
n = 15981 n = 5497
g
eGFR < 60
Survival Probability
IL-17A <25th Perc
IL-17A 25th-75th Perc
IL-17A >75th Perc
log-rank: p = 0.010
Time [years]
At risk
<25th: 534 521 507 482 452 425 391 194
25th-75th: 1273 1236 1200 1135 1072 997 920 462
>75th: 978 949 912 859 810 750 669 315
h
IL-17A
Model 1 p < 0.0001
Model 2 p = 0.0129
Model 3 p = 0.0445
Hazard ratio (95% CI) for all-cause mortality
i
Human cardiac fibroblasts
± HD / HC serum 10%
± AhRi
± αIL17A
24 h incubation
Analysis by qPCR
j
IL17RA Relative mRNA expression
HC HD HD αIL17A HD AhRi
k
COL1A1 Relative mRNA expression
l
COL1A2 Relative mRNA expression
m
ACTA2 Relative mRNA expression